Acta Materialia 166 (2019) 687–701

Contents lists available at ScienceDirect

Acta Materialia

journal homepage: www.elsevier.com/locate/actamat

Full length article

Rate limiting deformation mechanisms of bcc metals in confined volumes

D. Kiener [a, *], R. Fritz [a], M. Alfreider [a], A. Leitner [a, c], R. Pippan [b], V. Maier-Kiener [c]

[a] Department Materials Science, Chair of Materials Physics, Montanuniversität Leoben, Leoben, Austria
[b] Erich Schmid Institute of Materials Science, Austrian Academy of Science, Leoben, Austria
[c] Department of Materials Science, Chair of Physical Metallurgy and Materials Testing, Montanuniversität Leoben, Leoben, Austria

ARTICLE INFO

Article history:
Received 4 September 2018
Received in revised form
21 December 2018
Accepted 15 January 2019
Available online 18 January 2019

Keywords:
Size effect
Thermally activated processes
In-situ SEM
Deformation mechanism
Activation volume

ABSTRACT

The influence of microstructure on the strength scaling behaviour of ultrafine-grained bcc metals is investigated by scale-bridging experiments spanning four orders of length on tungsten and chromium. By performing macroscopic compression experiments, nanoindentation and in-situ micro-compression tests in a scanning electron microscope, the plastically deformed volume was thoroughly reduced until a transition from bulk behaviour to single crystalline deformation characteristics was achieved. The stress-strain behaviour and local sample deformation characteristics were related to apparent deformation mechanisms established for polycrystalline bcc metals. The influence of small dimensions, interfaces and free surfaces on the deformation behaviour is considered with respect to the single crystal situation. The increasing fraction of free surfaces in small volumes explicitly alters the strength scaling behaviour in dependence of the intergranular dislocation accumulation processes. Furthermore, thermally activated deformation was analysed based on rate- and temperature-dependent properties, such as strain-rate sensitivity and activation volume. To mechanistically interpret this data, a dislocation based model predicting the temperature dependent activation volume was developed. We find that thermally activated kinks control the rate dependent properties below the critical temperature for all length scales and microstructure states.

1. Introduction

Body-centred cubic (bcc) metals such as tungsten, molybdenum, chromium or iron are not only employed in classical engineering applications, a variety of them is also used in modern fields such as microelectronics, display technology, power generation or energy harvesting, to name a few. Most of these high-technology areas are strongly driven by miniaturization, thus not only the intrinsic properties of the materials are important, but also understanding the influence of confined volumes and high surface ratios is of utmost importance for predicting and improving the material performance.

Small-scale testing techniques such as nanoindentation or micro-pillar compression experiments are well suited to permit novel insights into the strength scaling behaviour in confined volumes. Since Uchic et al. [1] reported a size effect in focused ion beam (FIB) machined single crystalline (sx) compression samples [2], ex-situ tests as well as in-situ pillar compression experiments inside scanning electron microscopes (SEM) increased in popularity [3–6]. In recent years, the strength scaling behaviour of sx, face-centred cubic (fcc) [7–11] and body-centred cubic (bcc) [12–19] metals was extensively studied. Nowadays, it is established that the strength σ in such confined volumes can be fitted by a power-law scaling with the sample diameter as the base and n as the strength scaling exponent ($\sim d^{-n}$). Typical n-values for fcc metals are ~0.6. The mechanisms responsible for such a scaling behaviour are interpreted based on a single-armed source model by Parthasarathy et al. [20], while more detailed mechanisms are discussed in Ref. [21]. Notably, the crystal orientation, or more precisely the number of active slip systems [22–24], as well as dislocation density [25–27] were reported to additionally affect n. With respect to temperature-dependent behaviour, while fcc metals can be regarded as athermal [11], in bcc structures the strength scaling exponent is furthermore dependent on a thermal stress component, which limits the movement of screw dislocations via the kink-pair mechanism [28–30]. Metals such as tungsten exhibit a high

* Corresponding author. Jahnstraße 12, 8700 Leoben, Austria.
E-mail address: daniel.kiener@unileoben.ac.at (D. Kiener).

https://doi.org/10.1016/j.actamat.2019.01.020

thermal stress component at room temperature (RT), evidenced by rather low n-values of 0.2–0.4 [8,12,15,19,23,30]. Contrarily, bcc metals with rather low melting points (T_m) such as niobium or iron show reduced thermal stress components resulting in strength scaling exponents of 0.48 [30] and 0.59 [17], respectively. If thermal activation reaches about $0.2 \cdot T_m$, screw dislocations are not hindered by the Peierls potential anymore and propagate with the same velocity as edge dislocations [29]. At this critical temperature (T_C), the strength scaling behaviour in bcc metals approaches towards the fcc value [14].

The variation of n is not only controlled by intrinsic effects [7]. Beside varying thermal stress contributions, also extrinsic effects [31], preparation induced artefacts such as FIB damage [32–34], or processing induced modifications [35] may alter the strength scaling behaviour and must be taken into account.

To comprehensively study the effect of internal interfaces on the size dependent strengthening, experiments spanning from the macroscopic to the microscopic regime need to be performed for a constant grain size. Testing macroscopic samples commonly allows to obtain bulk properties. In fact, several tensile, compression and also simulation studies were conducted on sx [36–41] as well as polycrystalline samples [42–46] to address the interplay of intrinsic length-scale contributions to strengthening mechanisms in macroscopic volumes.

On the other hand, miniaturized testing techniques are capable to limit the number of involved interfaces and investigate related deformation mechanisms, for example, interaction of dislocations with twin boundaries [47] or grain boundaries [45,48–50]. It was previously shown that dislocations can be trapped within small sample volumes and pile-up at internal interfaces [51,52]. However, there is an ongoing debate how grain boundaries or general interfaces affect the strength scaling characteristics.

To contribute to this discussion, in this work the influence of interfaces on the deformation and strength scaling behaviour of ultrafine-grained (ufg) bcc tungsten and chromium is thoroughly addressed. The interplay of grain boundaries with confined volumes is investigated by consequently reducing the deformed volumes for a constant grain size until an sx state is achieved. Therefore, macroscopic compression tests, nanoindentation and in-situ pillar compression experiments are performed at various temperatures and strain-rates. The acting deformation mechanisms are analysed in terms of strain-rate sensitivity (m) and activation volume (v). Based on these insights we examine the influence of grain boundaries as well as the contribution of the thermal stress component on the strength scaling characteristics.

2. Materials and methods

To examine a possibly wide range in material characteristic, a large spread in intrinsic critical temperature is desired [29]. Thus, tungsten was chosen as the bcc metal with highest melting point and critical temperature, respectively. For the low temperature metal chromium was selected. Iron would have an even lower critical temperature, but depending on purity that might be even below room temperature, causing unwanted additional experimental challenges, as besides elevated temperature also cryogenic testing would be required [53]. The experimental details on chromium tested in a similar range of homologous temperatures were published earlier [45,54,55], and we will only discuss differences and similarities with the tungsten data presented in this manuscript later.

The sx tungsten was grown by electron beam zone melting [56] and examined previously micro- and macroscopically by Wurster et al. [57]. The crystal was aligned in either (100) or (110) orientation to test multiple slip orientations [36]. A lamella with about 1 mm thickness was cut using a diamond wire saw and subsequently ground and electro-polished to remove plastically deformed surface layers.

A forged sheet of ultra-high purity tungsten with an initial grain size of about 5 μm was provided by Plansee SE (Reutte, Austria). The as-received sample was cut by electron discharge machining (EDM, Brother HS-3100) to disks of 30 mm diameter and 7 mm height, and subsequently deformed via high pressure torsion (HPT [58–62]) to achieve an ufg microstructure with mostly large angle grain boundaries. After 10 rotations at 400 °C using a rotational speed of 0.2 rpm and an applied pressure of 4 GPa, an equivalent strain of ~7500% at a radius of 14 mm was imposed. A lamella as described in Ref. [63] and several rectangular-shaped macroscopic compression samples having final dimensions of $2 \cdot 2 \cdot 3$ mm^3 were machined by EDM from a disk radius of ~14 mm in axial direction of the HPT disk to avoid strain gradients and hence varying grain sizes within the macroscopic specimens. As for the single crystal, prior to any microstructural investigation, nanoindentation experiments or macroscopic compression tests, the bulk samples were mechanically and electrolytically polished.

The grain size was determined using back-scattered electron (BSE) images and electron backscattered diffraction (EBSD) grain orientation maps were collected with a high resolution field emission SEM (Zeiss LEO 1525, Oberkochen, Germany).

Non-tapered square-shaped pillars with side lengths in the range between 150 nm and 5 μm and an aspect ratio (pillar height to diameter) of 3:1 were milled out of the fabricated lamella using a dual-beam SEM-FIB workstation (Zeiss LEO 1540 XB, Oberkochen, Germany) [63]. Pillar compression tests on samples larger than 1 μm were performed in-situ in an SEM (Zeiss LEO 982, Oberkochen, Germany) equipped with an UNAT-SEM indenter (Zwick GmbH & Co. KG, Ulm, Germany) [64,65]. Samples having dimensions below 1 μm were tested in the SEM-FIB utilizing a Hysitron PI-85 Picoindenter (Bruker Nano Surfaces, Minneapolis, MN, USA). The indenters were equipped with conductive diamond flat punches obtained from Synton-MDP AG (Nidau, Switzerland), having diameters of ~8 μm and ~6 μm, respectively. All tests were performed at room temperature (RT) in displacement-controlled mode at constant displacement rates. These rates were adapted to the individual pillar geometry in order to achieve a constant nominal strain-rate of $3 \cdot 10^{-3}$ s^{-1} to exclude any potential strain-rate effects. Further corrections for sample sink-in [66] and machine stiffness [67] were taken into account. This is important in order to minimize errors associated with strain determination, as this is obtained from the recorded machine displacement rather than locally measured on the sample surface.

Macroscopic compression tests were performed in air using a universal tensile testing unit (Zwick GmbH & Co. KG, Ulm, Germany) modified with a load reverse tool to a compression device. To assess thermally activated processes, experiments were conducted at constant strain-rates between 10^{-2} s^{-1} and 10^{-4} s^{-1} for temperatures ranging between RT and 610 °C. Loads were measured utilizing a 10 kN load cell, and strain is calculated from recorded time and corresponding crosshead velocity, in analogy to the micro-compression experiments. All macroscopic and microscopic compression samples were deformed to about 20% engineering strain, and engineering stresses were calculated by dividing the recorded loads by the top area of pillars and macroscopic samples before deformation, respectively.

Nanoindentation tests were performed using a Nanoindenter G200 (KLA-Tencor, Milpitas, USA) equipped with a continuous stiffness measurement (CSM) unit. The CSM frequency was set to 45 Hz and a harmonic displacement amplitude of 2 nm was superimposed for all tests. The CSM signal was used to continuously record the contact stiffness to assess the Young's modulus

versus indentation displacement profile, which should be depth-independent for mechanically isotropic materials. For RT testing, a three-sided diamond Berkovich pyramid, imposing about 8% plastic strain (MicroStar Technologies, Huntsville, USA), as well as a diamond Cube Corner indenter, imposing about 20% plastic strain (Synton-MDP AG, Nidau, Switzerland) [68,69] were utilised. Rate controlled experiments with a constant strain-rate of $5 \cdot 10^{-2}$ s^{-1} were conducted to compare indentation stress to flow stress values obtained from uniaxial testing techniques. High temperature measurements were realized using a surface laser heating system with independent heating capacity of indenter tip and sample. Experiments were executed at 100 °C, 150 °C, 200 °C, 250 °C and 300 °C using a Berkovich pyramid tip made of sapphire (Synton-MDP AG, Nidau, Switzerland). Strain-rate jump tests [70] with displacement segments of 500 nm for each strain rate and to strain-rate levels of $5 \cdot 10^{-2}$ s^{-1}, 10^{-2} s^{-1}, $5 \cdot 10^{-3}$ s^{-1} (high temperature) and $5 \cdot 10^{-2}$ s^{-1}, $5 \cdot 10^{-3}$ s^{-1} and 10^{-3} s^{-1} (RT), respectively, were performed to investigate thermally activated processes. The maximum indentation depth for all indents was set to ~2500 nm, which is much deeper than the grain size of the material, thus ensuring sampling of bulk material properties. Machine stiffness and tip-shape calibrations were performed according to the Oliver-Pharr method [71], while further details about the heating setup are provided in Ref. [72].

3. Results

The grain size of the HPT deformed tungsten sample was determined using a line intercept method for the BSE images and by calculating the diameter of circles having identical areas as the grains determined by EBSD. For this analysis, boundaries among neighbouring grains exhibiting 15° misorientation or more were ascribed as large angle GBs. This resulted in average grain sizes of 530 ± 170 nm and 480 ± 230 nm for Fig. 1a and b, respectively. In the BSE image, substructures and low angle grain boundaries are not accounted as boundaries, resulting in a slightly larger average grain size. Moderately elongated grains in shearing direction are observed, but no pronounced texture was evident. Moreover, the grain boundary character was analysed, as shown in Fig. 1c. A large angle grain boundary fraction of 87.2% common for HPT deformation in the saturation regime was detected.

The bulk hardness (H) of the (110) oriented sx and ufg tungsten at RT was determined by nanoindentation using Berkovich and Cube Corner indenter tips. Corresponding load-displacement curves are shown in Fig. 2a. Note that for the Berkovich tests of ufg tungsten the indentation system's load limit was already met at around 1500 nm indentation depth. The related replaced volumes are 116.2 μm^3 (Berkovich) and 13.3 μm^3 (Cube Corner) for sx tungsten and 39.7 μm^3 (Berkovich) and 14.6 μm^3 (Cube Corner) for ufg tungsten, respectively. Hardness values were converted to flow stresses using $H = \sigma \cdot C^*$ with the constraint factor $C^* = 2.8$ [69,73]. For the single crystal, bulk values of H were obtained by extrapolating the depth-dependent hardness profile to large displacements according to the Nix and Gao model [74]. Although the moduli of sx (393 GPa) and ufg (402 GPa) tungsten show slight variations, they are well in the range of reported literature values of 380–420 GPa [75].

Hardness-converted flow stress values for sx tungsten resulted in 1470 MPa (Berkovich) and 1790 MPa (Cube Corner), while for the ufg material values of 3110 MPa (Berkovich) and 2930 MPa (Cube Corner) were obtained, which are in accordance with literature data, see Ref. [69] and references therein.

Fig. 2c and d present engineering stress-strain curves of (100) oriented sx and ufg tungsten, respectively. In both cases, large samples exhibit continuous flow curves. As the sample size decreases (below 3 μm), stress values in sx tungsten samples (Fig. 2c) increase due to the sample size effect and stochastic plastic events such as load drops are observed more frequently. A contrary behaviour is observed for the ufg tungsten samples (Fig. 2d), where the flow stresses decrease with decreasing sample sizes. At sample diameters of ~3 μm, first serrations in the stress-strain curves are discernible. Further decreasing the sample size leads to an apparent decrease of flow stress values and numerous pronounced load drops are detected, comparable to the discrete plastic events in small sx tungsten samples. Notably, the elastic stiffness of the macro-scale sample is reduced and not comparable to pillar experiments in Fig. 2d. Alignment of the bulk samples was hampered due to comparably low stiffness of the compression equipment, resulting in a potential sample misalignment of ~1°, thus only approximated strains are given for the bulk sample. However, due to the generally low strain hardening behaviour of ufg materials at plastic strains exceeding few percent [59], this does not significantly affect the analysis. Specific data for ufg tungsten is reported for example in Refs. [42,69], and this aspect will be corroborated in more detail later.

Post compression SEM images of various ufg tungsten specimens are shown in Fig. 3. In total 36 bulk samples each having a size of $2 \cdot 2 \cdot 3$ mm^3, as representatively shown in Fig. 3a, were tested from RT up to 610 °C. At low temperatures, independent of strain-rate, cracks occurred during compression. Above 450 °C, plastic deformation took place without obvious crack initiation and propagation. This characteristic is indicative of a rate- and grain size dependent brittle-to-ductile transition temperature (BDTT) [76,77]. Fig. 3b and c display residual Berkovich and Cube Corner impressions at RT,

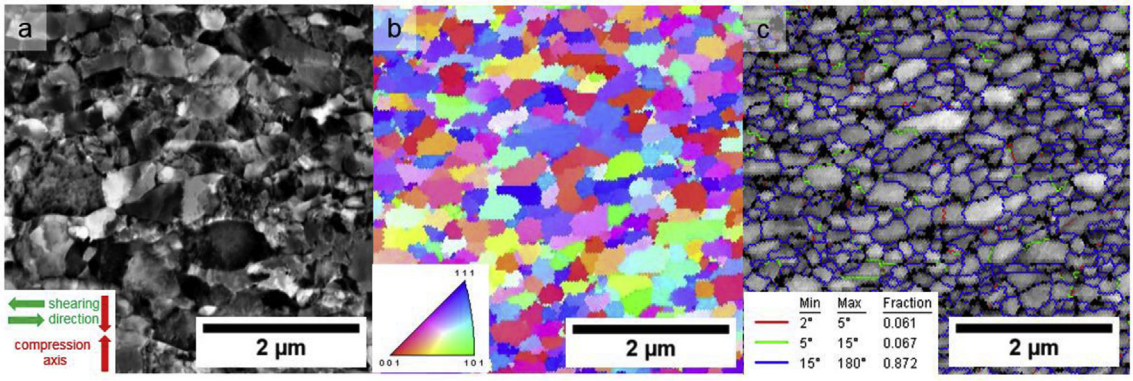

Fig. 1. Microstructure of ufg tungsten deformed by HPT at 400 °C at a disk radius of 14 mm in axial direction. (a) BSE image, red arrows indicate the compression direction and green arrows the shearing direction during severe plastic deformation. (b) EBSD image of the respective microstructure and the corresponding inverse pole figure. (c) The majority of grain boundaries (87.2%) have a large angle character. (For interpretation of the references to colour in this figure legend, the reader is referred to the Web version of this article.)

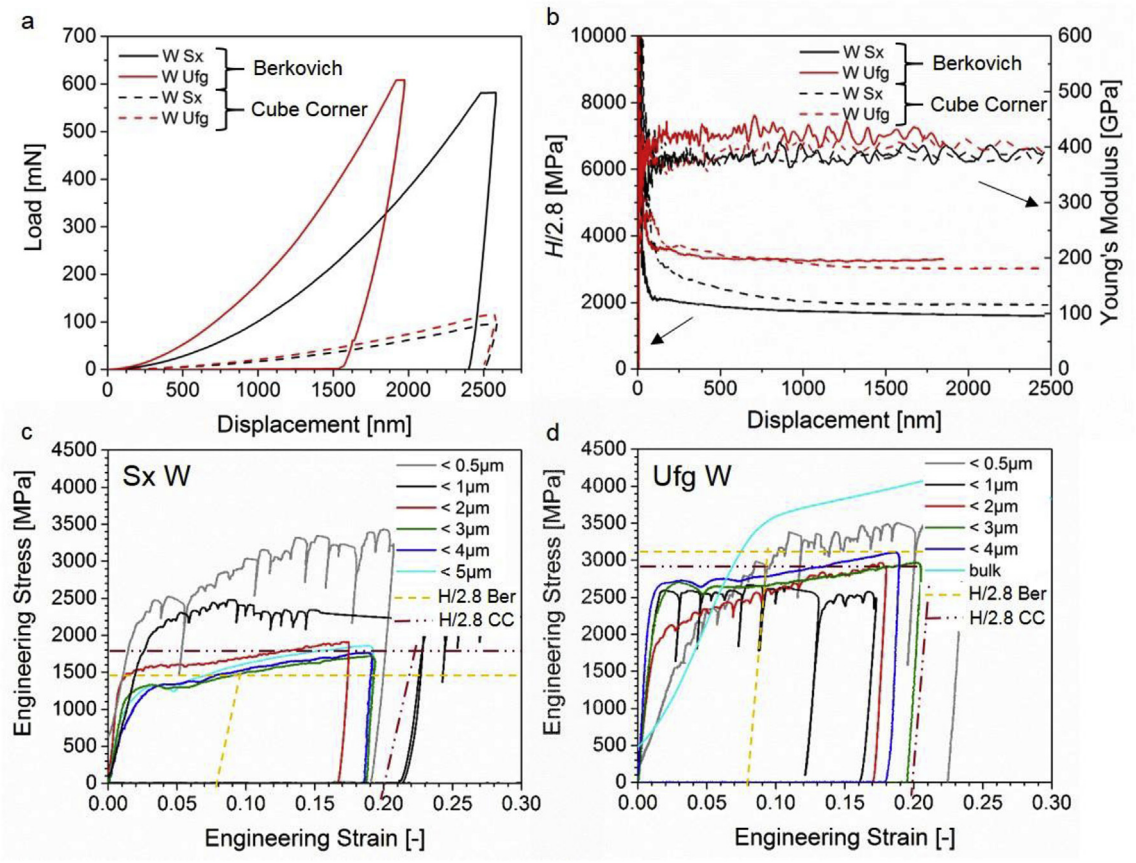

Fig. 2. Multi- and uniaxial mechanical data of sx and ufg tungsten determined using nanoindentation and compression tests. (a) Load-displacement curves obtained with Berkovich and Cube Corner indenters. (b) *H*/2.8 and Young's moduli vs. indentation depth. (c, d) Exemplary engineering stress-strain curves of the respective sx and ufg tungsten with a large variety of sample sizes. See text for details.

respectively. Fig. 3d–i depict deformed ufg tungsten pillars of various sizes. Larger pillars in Fig. 3d and e show indication of intercrystalline failure at grain boundaries, as common for ufg tungsten [78,79]. A sample side view and magnified details of Fig. 3d indicated by the red arrow and the rectangle are displayed in Fig. 3h and i, respectively. The white arrows highlight decohesion and local failure at grain boundary triple points, which were also observed within and around residual imprints (Fig. 3b and c). Fig. 3f represents an ufg pillar where the sample size approximately matches the grain size, while in Fig. 3g, due to the further sample size reduction, a single grain spanned the specimen cross-section. In this situation, localized plastic deformation determined by the crystallography is observed, as expected for a single crystal.

The local plastic deformation behaviour of sx and ufg tungsten is also provided in supplementary videos, where Video 1 represents the deformation behaviour of ~5 µm and ~0.3 µm sized sx tungsten pillars. Video 2 depicts the deformation characteristics of ~3 µm, ~1.3 µm and a ~0.3 µm sized ufg tungsten samples. In the larger ufg pillars, cracks developing at grain boundary junctions can be observed.

Supplementary videos related to this article can be found at https://doi.org/10.1016/j.actamat.2019.01.020.

Fig. 4 presents SEM images of etched (a) and FIB-prepared (b-g) cross-sections of deformed specimens. Fig. 4a shows a crack tip observed in a macroscopic sample. The varying surface pattern (points and triangles) for individual grains indicate etch pits resulting from dislocations that align perpendicular to the etched surface (estimated dislocation density ~$1.65 \cdot 10^{14}$ m^{-2}). The major crack propagated along an intercrystalline path, and additional small cracks are observable at grain boundary triple junctions, indicated by white arrows in Fig. 4a. The cross-sections in Fig. 4b–e displays deformed pillars. They exhibit polycrystalline deformation comparable to observations from the bulk samples, even though the number of grains in the deformed volume is drastically reduced. Once the sample size is dropped to the average grain size (Fig. 4f) or below (Fig. 4g), the probability for crack nucleation at grain boundary junctions decreases. This can be rationalized by considering that for a constant defect density, e.g. a fraction of all triple junctions, the absolute number of defect nucleation sites in the tested volume scales to the third power of the specimen size. Furthermore, the unconstrained deformation at the surface reduces compatibility stresses that would arise otherwise. Still, a detailed statistical treatment is complicated by the fact that most of these defects are internal and cannot be assessed from surface observations. Pronounced single slip crystal plasticity is observed for the smallest pillar (300 nm, Fig. 4g), where a discrete localized slip step, highlighted by the green arrow, emerged within an individual grain as dictated by local crystallography.

To assess the influence of the tested volume on the mechanical properties, the flow stress is plotted against the plastically deformed volume of individual experiments in Fig. 5. For macroscopic and microscopic uniaxial compression tests, the plastically deformed volume is given by the sample base area and height. Considering the different indentation geometries, a simplified hemispheric plastic zone after penetration to maximum displacement was assumed [74]. Stresses at 8% plastic strain were chosen to allow comparison with Berkovich nanoindentation data and to include occurring strain hardening, as will be discussed later. Pillar

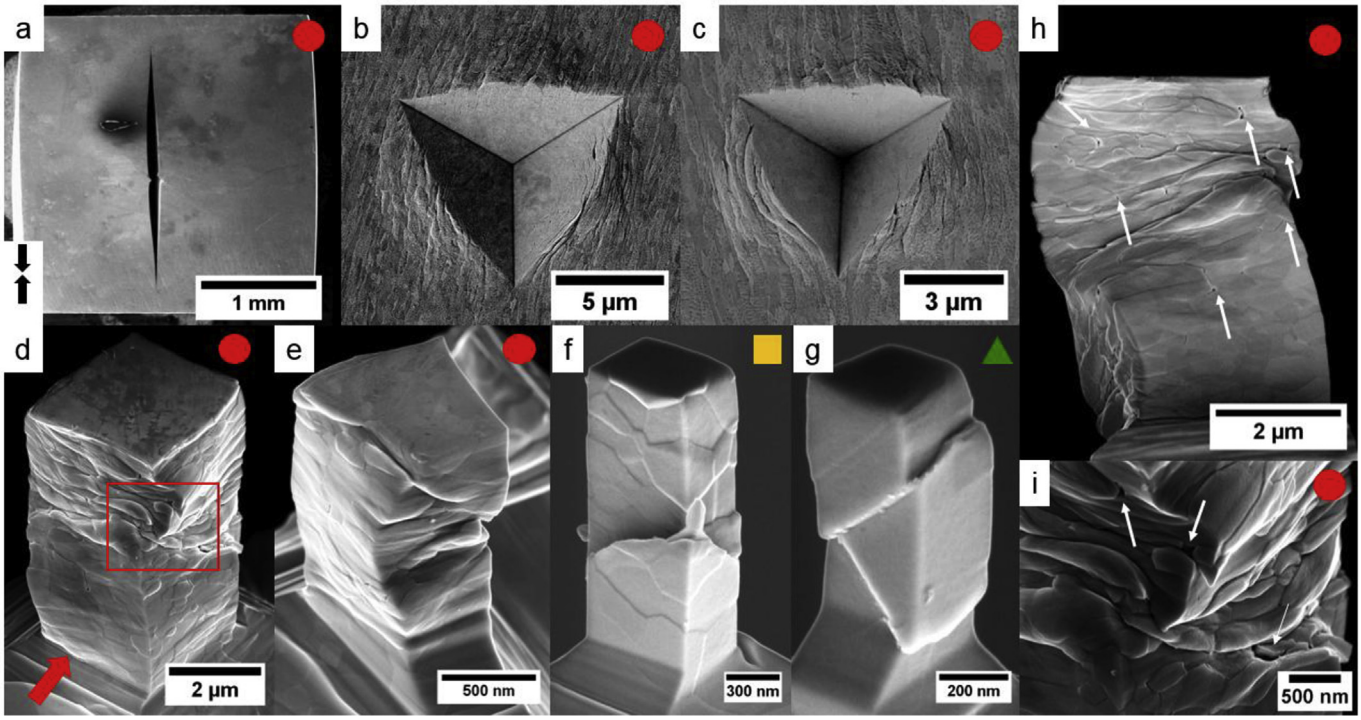

Fig. 3. Post-compression SEM images of various ufg tungsten samples. The sample size decreases in alphabetic order. (a) Deformed bulk sample (strain-rate of $2 \cdot 10^{-3}$ s^{-1}) with a splitting crack in compression direction (black arrows). (b) and (c) display Berkovich and Cube Corner indents, respectively. Micrographs (d) to (g) present deformed pillars with decreasing size. (h) and (i) highlight details indicated in (d), where white arrows point out interface decohesion events at grain boundary triple junctions. Coloured symbols refer to different deformation characteristics as detailed in the text. (For interpretation of the references to colour in this figure legend, the reader is referred to the Web version of this article.)

compression and nanoindentation data of sx tungsten is indicated by black dots and black triangles, respectively. The black line is a linear fit to the sx tungsten data, demonstrating its strength scaling behaviour as 0.21 ± 0.02 for the (100) orientation, in excellent agreement to previous investigations [23,30], as well as the transition to bulk behaviour at about 3 µm sample size (or roughly 80 μm^3 tested volume).

The deformation behaviour of the ufg tungsten data in Fig. 5 is separated into three different regimes. Red, orange and green symbols (also used in Figs. 3 and 4) indicate bulk behaviour, a transition regime in which the sample size approaches the grain size, and an sx-like region. In the latter situation, even though the tested pillar encompasses several grains, crystallographic slip planes in individual grains can span the whole cross section. Consequently, the specimen can deform by localized crystallographic single slip within this individual grain, comparable to the sx tungsten pillars, respectively. As these discrete straight slip traces are easily distinguishable by SEM imaging, the differentiation between the specific regimes is based on the individual deformation morphology of tested samples observed during in-situ testing and post inspection (e.g. Figs. 3 and 4), and further does not significantly depend on the amount of plastic strain. Upper bound error bars in Fig. 5 are derived from the out-of-contact noise of the indenter load signal and uncertainties in determining pillar cross sections to compute stress values.

As previously shown in Fig. 2d, ufg bulk tungsten samples reveal the highest flow stress levels. By decreasing the plastically deformed volume below about 10.000 μm^3, these values gradually decrease until the transition regime in Fig. 5. Upon further reducing the sample dimension, sx deformation behaviour is evidenced, as expected for a situation where individual grains span the whole sample cross-section.

To expand the data pool and allow comparability to earlier works in terms of strength scaling, open symbols in Fig. 5 indicate literature data of (100) oriented sx tungsten. From the present data and literature reports, flow stress values were extracted at various amounts of plastic strain. The variations in scaling behaviour are summarized in Fig. 6a by comparing n-values for strains ranging from close to the yield point up to 10% plastic offset strain. The present data (black symbols) is indicative for a constant strength scaling behaviour with strain, implying that the deformation characteristics do not markedly change with the amount of imposed plastic deformation. Slight variations between individual strain values are primarily attributed to alignment uncertainties at low strains and serrated flow at increased strain levels.

The strain hardening characteristic of the different microstructures and probed volumes was assessed by calculating strain hardening rates (Θ) from engineering stress-strain curves using a tangent approach from 2% up to a maximum offset strain of 10%. A comparison of macroscopic polycrystalline compression tests and different size ufg and sx pillars, classified by the apparent deformation mode and using the same colour code as in Fig. 5, is shown in Fig. 6b. All ufg pillars that exhibited a bulk deformation behaviour (indicated as “Bulk-like”) show comparable Θ as observed for macroscopic samples over the whole analysed strain range. However, once the sample size is reduced to the order of the grain size, the deformation characteristic changes to localized slip with the emergence of discrete slip planes on the surface (Fig. 4), and the samples exhibit reduced strain hardening behaviour (labelled “Sx-like”), since dislocations can easily exit on the pillar surface. In accordance, the strain hardening data of the sx-like ufg samples closely matches the values from the truly sx tungsten pillars.

To assess the thermally activated processes controlling plasticity, the values of strain rate sensitivity m and activation volumes

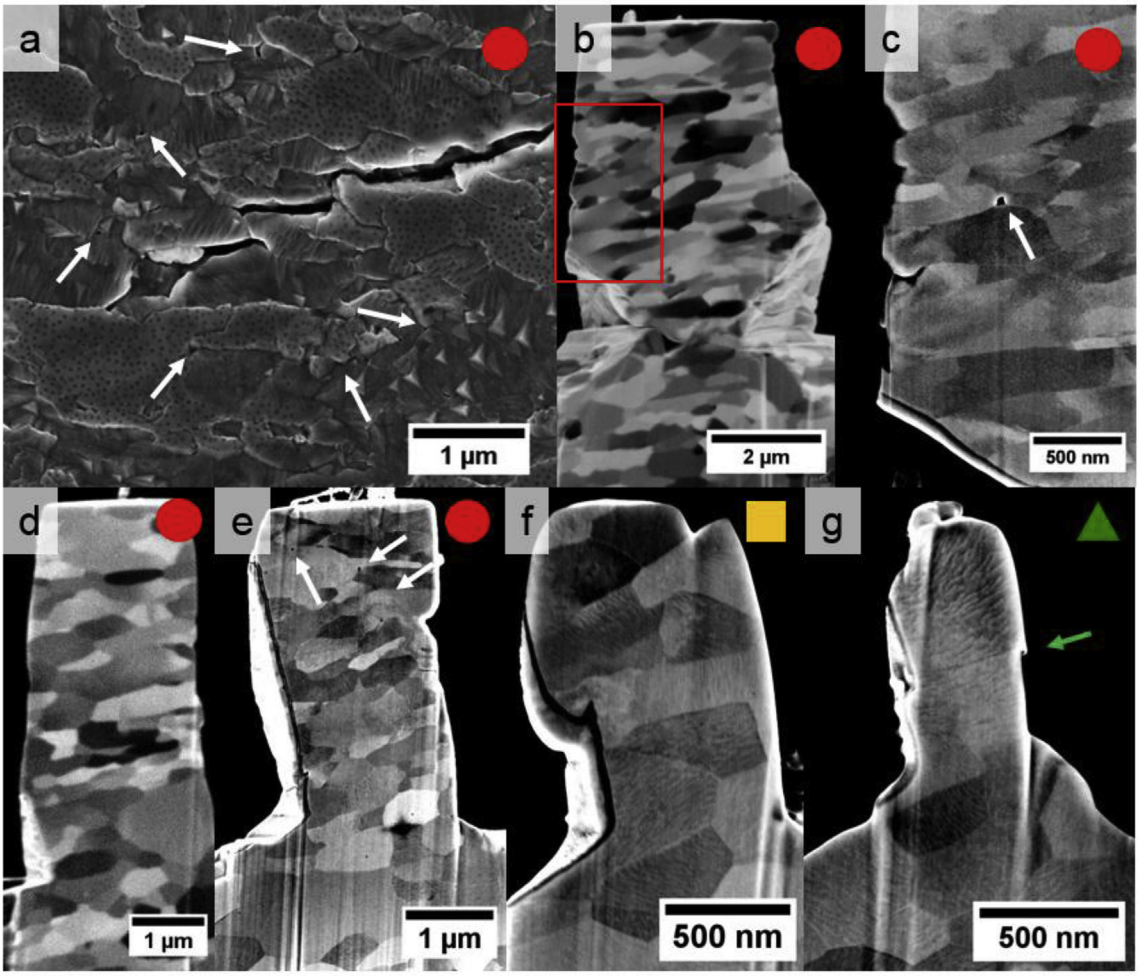

Fig. 4. Cross-sections of uniaxial deformed compression samples. (a) Crack tip observed in a macroscopic sample, indicating intercrystalline fracture. Pillar cross sections of 3 µm (b), 2 µm (d), 1.3 µm (e), 0.7 µm (f) and 0.3 µm (g) demonstrate the decreasing number of grains within and across individual samples. (c) provides a magnified inset of the area indicated by the red rectangle in (b). White arrows indicate internal cracks and decohesions at triple points of grain boundaries, while the green arrow marks a slip step. Coloured symbols refer to different deformation morphologies as explained in the text. Please note that the cross-sectional FIB cuts are slightly inclined compared to the pillar compression direction. (For interpretation of the references to colour in this figure legend, the reader is referred to the Web version of this article.)

ν were derived using the common equations, described e.g. in Ref. [80], and are plotted as a function of the testing temperature normalized by the critical temperature (T_{Test}/T_C) in Fig. 7a and b, respectively. The purpose of this normalization is to compare bcc metals that exhibit different thermal stress components at RT. The critical temperatures for tungsten and chromium in Fig. 7 were taken as 800 K [39] and 430 K [29], respectively. To compare the apparent activation volumes based on the varying microstructure in Fig. 7b, the corresponding ν-values were normalized by the cubed Burgers vector of the respective metal ($b_W = 2.741 \cdot 10^{-10}$ m and $b_{Cr} = 2.5 \cdot 10^{-10}$ m) and again plotted vs. T_{Test}/T_C. Another good reason to include the chromium data besides the different thermal contributions is that we were not able to exceed the critical temperature for the sx tungsten by nanoindentation in the present work. However, as both bcc metals should exhibit related deformation mechanisms, the sx chromium data serves to demonstrate the general behaviour. Moreover, low temperature data on coarse grained bulk chromium with 95 µm grain size from RT down to liquid nitrogen was additionally added from Ref. [81] to enlarge the discussed range of relative temperatures. The tungsten data reported in Ref. [39] was not included, as in that case stress relaxation tests were employed to obtain m-values. Nonetheless, a comparable trend was observed for sx tungsten.

The coloured arrows in Fig. 7a and b indicate the trends in rate-dependent properties in the two bcc metals. They reveal comparable characteristics in sx and ufg tungsten and chromium, respectively. Importantly, in the chromium study [55] no cracking was observed. This permits to exclude fracture and thus embrittlement of GBs via segregation of interstitial atoms [82] as a dominant influencing mechanism.

4. Discussion

The purpose of this discussion is to initially establish comparability between the different experimental techniques used. Based on this, the observed size and microstructure dependent material strengthening will be discussed. Finally, we address the underlying rate and temperature dependent deformation mechanisms of the two bcc metals in a mechanistic picture and generalize this by developing a model based on dislocation kinks that correctly predicts the measured temperature dependent activation volumes.

4.1. Comparability between compression and indentation experiments

Before comparing the macroscopic and microscopic uniaxial

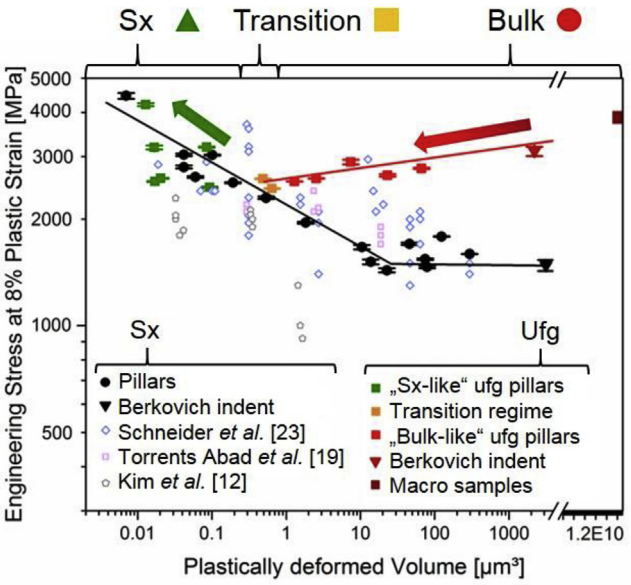

Fig. 5. Engineering stress at 8% plastic strain vs. plastically deformed volume of respective tests on sx and ufg tungsten. Filled symbols indicate data from this work, while open symbols are literature data on sx tungsten, respectively.

stress data to the multiaxial indentation results, some related considerations should be made. Nanoindentation using self-similar pyramidal tips results in multiaxial stress-states underneath the indent, accompanied by multiple slip events and corresponding occurrence of dislocation interaction processes. To facilitate comparison with uniaxial test data, the (100) single crystal orientation was chosen for pillar compression tests, as this multiple slip orientation also promotes dislocation interaction events. In the case of polycrystalline micro-samples, local compatibility will require deformation to take place on multiple slip systems, just as in the macroscopic situation. Further, to relate from hardness to a representative flow stress, the choice of an appropriate value for C^* can influence validation of the uniaxial test data. However, even if C^* would be considered to be in the range of 2.5–3, rather than a value of 2.8 as used in Fig. 2, the resulting change of hardness-derived stress values of about 10% would only insignificantly affect present results. Lastly, the Young's modulus to hardness (E/H) ratio [83] and the rate-dependence of the tested material [84] might affect the load response of the nanoindenter, resulting in conceivable errors. The E/H ratio for the investigated ufg tungsten is ~130, therefore, a possible phase shift of the indenter signal as reported in Ref. [83] should be only of minor influence. To eliminate effects relating to the rate-dependence of the material, all experiments were conducted at the same constant engineering strain-rates.

Furthermore, the plastically deformed volumes during nanoindentation vary with the indenter geometry and mechanical properties of the sample [85,86], which is apparent in the load-displacement data in Fig. 2a. However, as long as the contact stiffness is properly accounted for (indicated by depth-independent Young's modulus values in Fig. 2b) the test can be considered valid. In Fig. 2b, a cross-over of the depth-dependent hardness signals of the Berkovich and Cube Corner indent is observed for ufg tungsten. As mentioned before, hardness values depend on the indenter geometry, as the induced representative strain scales with the tip opening angle [68], where the Cube Corner tip features a high strain of about 20% compared to Berkovich indentation ($\varepsilon \approx 8\%$). For coarse grained or single crystalline materials with pronounced work-hardening (see Fig. 2b), naturally higher hardness values are measured using a Cube Corner tip. For materials with refined microstructures comprehensive investigations demonstrated that this behaviour changes, as local stress induced softening will reduce and even exceed any occurring hardening [69,87]. Notably, Fig. 2b underlines this previous finding on ufg tungsten, as the hardness level of Cube Corner indentation is well below that of Berkovich measurements at high displacements.

The gap in flow stress values between sx and ufg tungsten results from microstructural refinement according to the well-known Hall and Petch behaviour [88,89]. Estimation of the yield stress using a friction stress of $\tau^* = 345$ MPa [8], a mean grain size of 480 ± 230 nm and a Hall-Petch coefficient of 1.86 MPam$^{-1/2}$ [69] results in ~3000 ± 700 MPa, which is in agreement with the ufg tungsten bulk data obtained from macroscopic compression tests and nanoindentation data (Fig. 2d).

4.2. Size dependent strength and deformation characteristics

After establishing comparability between the data gathered over several orders of magnitude, we will address the influence of

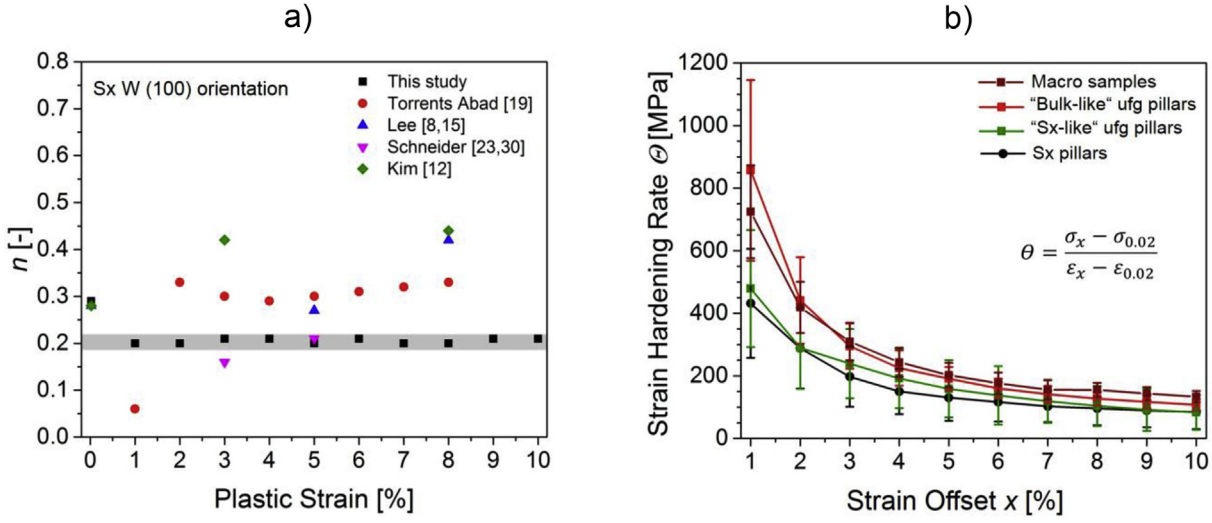

Fig. 6. (a) Strength scaling exponent n plotted against plastic strain and comparison with literature data. (b) Strain hardening rates Θ obtained from sx and ufg tungsten using a tangent approach (inset). Clear differences in Θ between bulk and sx deformation configurations are evident.

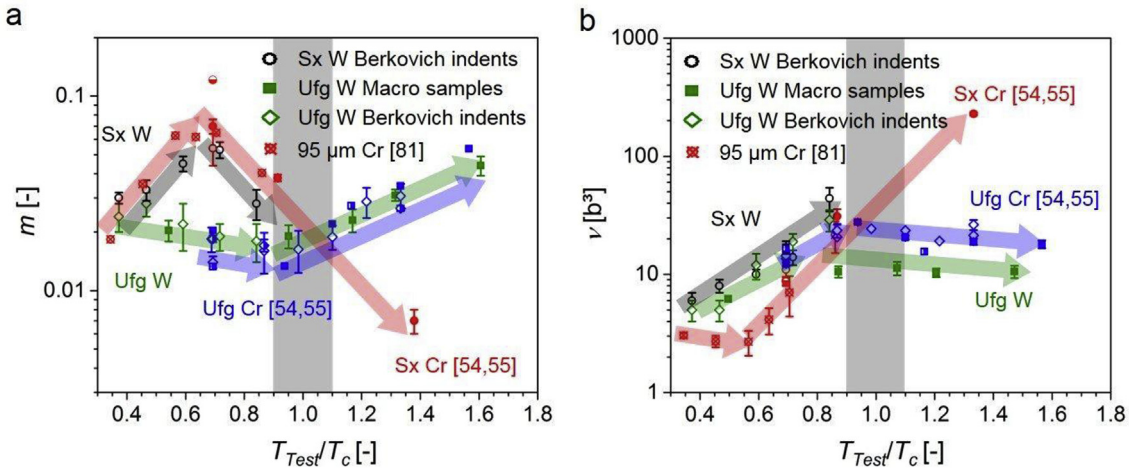

Fig. 7. Evolution of strain-rate sensitivity m (a) and activation volume ν (b) with respect to a normalized temperature for tungsten and chromium. Chromium data was taken with permission from Refs. [55,81]. Coloured arrows indicate trend lines. (For interpretation of the references to colour in this figure legend, the reader is referred to the Web version of this article.)

tested volume on strength and deformation morphology.

While the gradual transition from bulk to single crystal behaviour in Fig. 5 is not surprising, the decreasing flow stresses for reduced sample size are somewhat unexpected and require further attention. Considering the dislocation content within the grains, for the present average diameter of about 500 nm (Fig. 1), intergranular dislocation content developed during the initial HPT deformation process remains within the grain interior, as evident from the contrast variation within individual grains in the BSE micrograph in Fig. 1a. Grains mostly free from dislocations would only be expected for diameters below about 200 nm [90,91].

During plastic deformation of the ufg tungsten, dislocation sources within the grains will form from this initial intergranular dislocation content, operate and emit dislocations, which subsequently pile-up at grain boundaries that block their glide [92–94]. Such behaviour is commonly accepted for bulk deformation [88,89]. Contrarily, in grains located at free surfaces, dislocations originating from the synthesis as well as those generated during micro-mechanical testing can easily exit at the free pillar surface [95], which leads to a reduced back stress acting on the active dislocation source. These behaviours have recently been reported also for confined volumes using in-situ TEM experiments as well as simulations, see for example [51,92,96,97]. Specific references to tungsten can be found, for example, in Refs. [79,98].

Essentially, the annihilation of dislocations and resulting reduction in back-stresses comparatively decrease the flow stress level for these surface grains compared to confined bulk grains.

With decreasing sample size, the relative fraction of surface grains rises for a fixed grain size, a fact well described by analytical models [99,100]. Hence, the overall flow stress of the miniaturized structure decreases until the sample size approaches the grain size and source-controlled strengthening [20] controls plasticity. Expectedly, the point of intersection between the strength trend lines of sx and ufg tungsten in Fig. 5 correlates reasonably with the ufg grain size.

4.3. Relation to observations on sx and ufg chromium

Related experiments were conducted on ufg chromium pillars containing mostly large angle GBs, reported in Ref. [45]. Different to the softening reported here, a continuous increase of flow stress was observed by decreasing the sample size. Notably, the average grain size for ufg chromium was ~160 nm [45]. As outlined above, within such fine microstructures, GBs act as sinks and sources for dislocations [101], while the grain interior contains only a very limited number of dislocations [92]. In such a situation, grains located at the free surface remain stronger than internal ones, since stress concentrations occurring at triple points and along grain boundary junctions promote dislocation nucleation compared to smooth free surfaces. Thus, for the case of low or non-existent internal dislocation content, a scaling behaviour with smaller samples being stronger results.

Notably, in the present ufg tungsten as well as for the 160 nm chromium [45] near-surface grains are smaller on average compared to internal grains, which results from the FIB machining that carves the pillar out of the bulk material. However, within the available data this truncation of grain sizes at the surface seems to be of minor influence for the observed behaviour.

The dislocation structure in the grain interior affects the size dependent strengthening behaviour in terms of accumulation in ufg tungsten versus exhaustion in ufg chromium [45], in agreement with previous discrete dislocation simulations [21]. Thus, it is commensurate to assess the influence of plastic strain on this behaviour and any conclusions drawn. Starting with the strength scaling behaviour of sx tungsten shown in Fig. 6a, n-values ranging between 0.2 and 0.4 were reported previously [8,12,15,19,23,30]. The present data shows no pronounced dependence on strain and is in close agreement to Schneider et al. [23,30], while the differences to other works on sx tungsten could be related, for example, to dissimilar applied strain-rates, a varying impurity content, or different initial dislocation densities [21] within the samples used in those studies.

Turning to the polycrystalline samples, it was shown previously using miniaturized bending beams that the presence of a single grain boundary within the specimen can have a profound influence on the dislocation pile-up behaviour compared to the single crystal situation without obstacles [102]. In the present work, dislocations in large ufg tungsten pillars pile-up at grain boundaries just as they would for macroscopic compression tests. However, the reduction in sample size goes hand in hand with a reduction of internal obstacles, which might affect the strain hardening behaviour in the sample interior and therefore the deformation behaviour.

The data in Fig. 6b compares strain hardening rates for macroscopic as well as microscopic samples. Evidently, polycrystalline ufg pillars still exhibit a work hardening rate in accordance to macroscopic tests. However, once discrete single crystal slip is observed for small ufg samples (sx-like ufg pillars), the work hardening rate drops

to the lower values generally exhibited by sx tests. These trends are consistent within the analysed plastic strain regime. Thus, we can state that there is no distinct difference in the dislocation accumulation behaviour between the experiments performed at different length scales as long as deformation characteristics are alike.

4.4. Temperature and microstructure dependent deformation processes

To relate the observed deformation behaviour to the underlying mechanisms and distinguish possible contributions from dislocation slip, decohesion, failure, or grain boundary sliding [103,104], intrinsic deformation mechanisms can be inferred based on the strain-rate sensitivity (m) and apparent activation volume (ν) of the material [28,105]. For sx and polycrystalline fcc metals such as nickel, aluminium or copper, strain-rate effects were investigated, for example, in Refs. [106–109]. Prevailing deformation mechanisms in bcc metals such as vanadium, tungsten, molybdenum, tantalum and chromium inferred from transient experiments were reported by Wei et al. [80,110], Zhou et al. [111], Wu et al. [101], Maier et al. [54,112], Choi et al. [113] and Fritz et al. [55].

In Ref. [55], we obtained thermally activated deformation behaviour for sx and ufg chromium in a wide range of temperatures using different testing techniques over several length scales, and comparable experiments were conducted within this work on tungsten. The normalization in terms of a relative temperature collapses the two material characteristics, facilitating a discussion of their equivalent deformation behavior. Concerning the strain rate sensitivity in Fig. 7a, at low relative temperatures m-values for sx chromium and tungsten amount to ~0.02. Initially, an increase of m is evident with increasing temperatures, until peak m-values of ~0.07 are reached at $T_{Test}/T_C = 0.65$. A comparable trend for low temperature deformation of sx tungsten, niobium, vanadium, and tantalum was reported by Brunner and Glebovsky [39] and Christian and Masters [114]. This initial increase in strain rate sensitivity is commonly related to the thermally activated interaction of dislocation kinks with interstitial atoms, see e.g. Refs. [39,105,114]. Approaching and overcoming T_C, thermal activation eases the movement of kinks until m-values in the order of 10^{-3} are reached, as common for low Peierls potential materials such as fcc metals [54]. Contrarily to that, for ufg counterparts m-values slightly decrease from low temperatures until T_C, followed by a continuous increase up to a relative temperature of 1.6. This trend of a diminishing m below T_C for the ufg material compared to the sx state is emerging from the increased athermal strength, resulting from grain refinement, with respect to the thermal stress component. Overcoming the critical temperature, the strain rate sensitivity raises due to increased thermally activated accommodation of dislocations at grain boundaries, as detailed in Refs. [54,109].

Regarding the apparent activation volumes, at low temperatures, ν-values of 4–7 b^3 were derived for sx tungsten and chromium. Those quantities are indicative of a kink mechanism, which is dominant in bcc metals at low temperatures [29]. Notably, ν seems to remain constant in the macroscopic sx chromium tests at low temperatures until $T_{Test} = 0.55 \cdot T_C$, while it gradually increases in sx and ufg tungsten, as well as ufg chromium, respectively. A plausible explanation for this behaviour is that thermal activation of kinks might be hindered by interstitial atoms. This is supported by a pronounced yield strength observed in tensile stress-strain data in Ref. [81]. As stated earlier, comparable trends in activation volume were also reported for sx tungsten, niobium, vanadium and tantalum in Refs. [39,114] and related to interaction of kinks with impurities. Additionally, m- and ν-values from Ref. [81] were calculated at the lower yield point, while nanoindentation data and test data from compression experiments were evaluated at a plastic strain of about 8%, which might cause slight differences.

Generally, it can be stated for both materials in either microstructural condition that with increasing temperature impurities are no effective obstacle anymore. Then, the movement of kinks is eased by thermal activation, as indicated by an increase of the activation volume in Fig. 7b. Overcoming T_C for the sx materials results in ν-values of ~200 b^3, indicative of dislocation-dislocation interaction, a common mechanism observed in fcc metals [105].

In ufg tungsten and ufg chromium the activation volume increases at relative low temperatures comparably to the sx states, indicating again a rate-limitation based on the propagation of kinks. However, upon exceeding T_C, ν-values remain rather constant at ~20 b^3, typical for dislocation-grain boundary interactions, as previously reported for ufg chromium [45,54,55].

Based on the analysis of the ufg tungsten data and facilitated by the comparison to chromium in Fig. 7, we can acquaint that in the investigated temperature range dislocation mediated plasticity acts as the dominant deformation mechanism in sx and ufg tungsten, respectively. The crack formation observed in ufg tungsten at low temperatures (Fig. 4) natively affects the load bearing capability of the material (Fig. 5), but seems to be of minor influence on the underlying plastic deformation mechanisms. Rather, cracking is a consequence of the ongoing plasticity and incompatibility stresses resulting thereof.

4.5. Modelling the temperature dependent activation volume

To emphasize the validity of the mechanistic picture provided above, we developed a model to predict the activation volume as a function of temperature. The full details of this derivation are given in the appendix, at this point we will just provide the essential assumptions and approach used.

To derive expressions for the stress-dependent activation volume, we follow the work of Caillard and others and split the deformation behaviour in a low temperature regime governed by the critical bulge mechanism, and a high temperature regime governed by an interacting kink pair up to the critical temperature [115–117], see Fig. A1. For simplicity, we use classical dislocation theory with an Eshelby potential [118]. Based on this, we can derive analytical expressions for the activation volume depending on the kink height and the temperature dependent Peierls stress (see equations A2 and A8). The temperature dependence of the Peierls stress is described by upper and lower bound scaling relations (equation (A11)) based on literature data following ideas of Suzuki et al. [119], as shown in Fig. A2 using data from Refs. [119–125]. Finally, the kink height can be calculated from the slip geometry for all possible slip systems [126]. The result is shown in Fig. 8 in comparison to experimental data from our work on chromium and tungsten. The light shaded areas not bound by black lines indicate the temperature regime where the models are not strictly valid anymore.

Evidently, the data for macroscopic as well as microscopic experiments is well described by the model. An upper bound to the activation volume is set in the low temperature regime by a critical bulge configuration, while the high temperature data falls well within the range of interacting kink pairs on the expected {$\bar{1}$12} <111> slip system. The {$\bar{1}$23}<111> and {011}<111> slip systems indicated by dashed lines would give too high and low boundaries, respectively.

The lateral extent of these kink pairs remains in the order of 10 nm for $\nu \approx 70\,b^3$, which is small compared to the grain sizes of 160 nm and 500 nm for chromium and tungsten, respectively. Thus, we can model the data well, without the need of taking grain boundary interactions into account, the simple and elegant dislocation kink picture is sufficient.

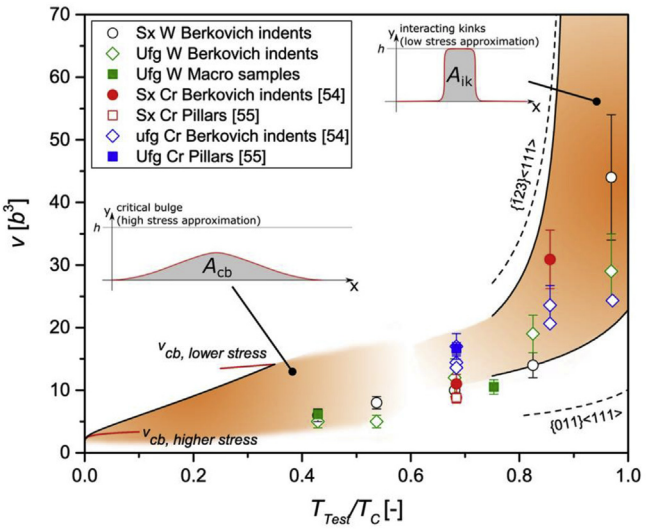

Fig. 8. Temperature dependent prediction of the activation volume based on the kink interaction and critical bulge models in comparison to the experimental data.

5. Conclusion

Interface-dominated strength scaling behaviour in single crystal and ultrafine-grained tungsten and chromium was examined over several length scales to investigate the interaction of dislocations with grain boundaries and free surfaces macroscopically and in confined bcc structures.

To understand the sample size dependent strengthening, the evolution of dislocation structures within the different grain sizes and the interplay of grain size with sample size has to be taken into account. Depending on this, the increasing fraction of surface grains can give rise to a size dependent strengthening, as observed for chromium, or a weakening, as seen for tungsten. For very small samples in the range of the grain size, single crystalline slip is activated in individual grains spanning the cross-section of the ufg pillars.

The influence of decohesion occurring at grain boundary triple points in tungsten on rate limiting deformation processes was examined and compared to ultrafine-grained chromium, where cracking was absent. No noticeable influence of crack nucleation or decohesion processes on the rate-dependent deformation characteristics was evident. Mechanistically, in both materials interfaces have a decisive role on the deformation behaviour above the critical temperature via dislocation-grain boundary interactions, as indicated by constant activation volumes in that regime.

Finally, a temperature dependent model of the activation volume based on dislocation kinks valid up to the critical temperature was developed. It shows that the rate limiting deformation mechanism in all investigated microstructures can be explained by dislocation kinetics rather than a complex dislocation-grain boundary interaction below the critical temperature.

Given the comparable behaviour of chromium and tungsten despite their vastly different melting points, it seems adequate to suggest generalization of this behaviour for all bcc metals.

Acknowledgements

The authors want to thank DI Peter Kutleša for help during sample preparation with the HPT device. Financial support by the Austrian Federal Government represented by the Austrian Science Fund FWF (project number: P25325-N20) is gratefully acknowledged. Additional funding of this work was provided by the Styrian and the Tyrolean Provincial Government, represented by Steirische Wirtschaftsförderungsgesellschaft mbH and Standortagentur Tirol, within the framework of the COMET Funding Programme (837900, MPPE A7.19). D.K. and R.P. further acknowledge funding by the European Research Council under Grants number 771146 (TOUGHIT) and 340185 (USMS), respectively.

Appendix

The classical analytical models for double kink nucleation developed in the 60s-70s are usually split into two regimes. For a low applied shear stress τ the energy of a kink pair is approximated by the sum of the energy of two well separated kinks and their elastic interaction [115,116]. For a high applied shear stress on the other hand the energy is approximated by the line tension of a critical bulge configuration [115,117,127]. Both model assumptions are depicted schematically in Fig. A1, where the red lines are the specific dislocation segments, h is the kink-height (distance to the next Peierls valley), ΔE is the Peierls barrier height and A_{ik} and A_{cb} are the respective activation areas with $A=v/b$, where v is the activation volume and b is the Burger's vector.

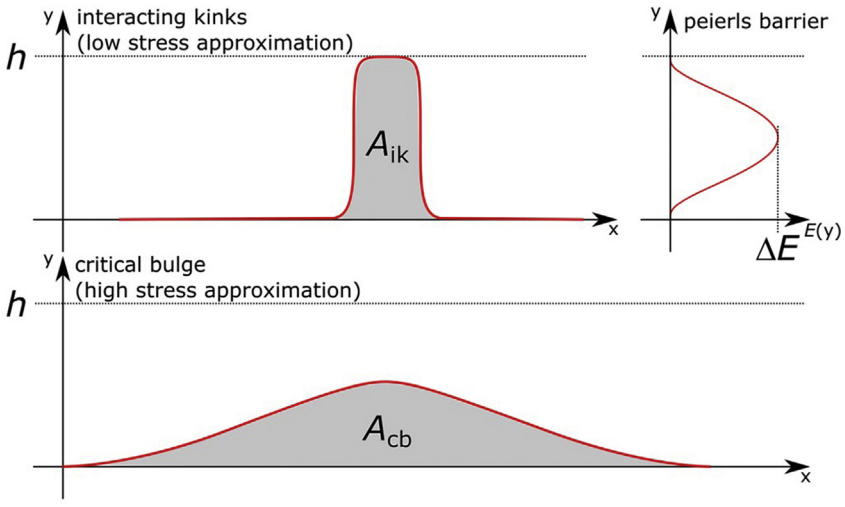

Fig. A1. Schematic representation of the interacting kinks configuration (above) and the critical bulge configuration (below) of a dislocation line to move from a Peierls valley to the next.

Interacting kinks (Low stress approximation)

Following the assumptions of Eshelby [118], as summarized by Caillard [115] based on detailed calculations from Hirth and Lothe [116] and Seeger [117], the activation area of two interacting kinks is:

$$A_{ik} = h\left(\frac{hb}{8\pi}\frac{\mu}{\tau}\right)^{1/2} \tag{A1}$$

with μ being the shear modulus. The Peierls stress τ_p for bcc materials is on the order of $2-8\times10^{-3}\ \mu$, with the majority around $5.5\times10^{-3}\ \mu$ [128]. Assuming $h = fb$, with f being a geometric pre-factor depending on the activated slip-system, and the stated τ_p -μ relation one deduces:

$$v_{ik}\left[b^3\right] = 2.69f^{\frac{3}{2}}\left(\frac{\tau_p}{\tau}\right)^{\frac{1}{2}} \tag{A2}$$

independent of the details of the assumed Peierls potential.

Critical bulge (High stress approximation)

The critical bulge configuration can be described using a line tension approach [117,127,129]. Using approximations that are only valid for $y_{max} \approx h$, *i.e.* for a large critical bulge at the lower end of the high stress regime, Seeger [115,117] derived an approximate solution for the activation area:

$$A_{cb} = h\sqrt{\frac{\widehat{T}}{E''(h)}}\left(1 + ln\left(\frac{\widehat{\tau}}{\tau}\right)\right) \tag{A3}$$

where $\widehat{T}$ is the line tension, which can be estimated with $\mu b^2/2$. $E''(h)$ is the curvature of the Peierls potential near its minimal value and $\widehat{\tau}$ is a stress constant. For an Eshelby potential these values are [115]:

$$E''(h) = \frac{32}{h^2}\Delta E;\ \widehat{\tau} = 12\sqrt{3}\tau_p = 64\frac{\Delta E}{hb} \tag{A4}$$

which leads to:

$$v_{cb,\ lower\ stress}\left[b^3\right] = 2.96f^{\frac{3}{2}}\left(4.03 + \ln\left(\frac{\tau_p}{\tau}\right)\right) \tag{A5}$$

for the activation volume of a critical bulge on the lower end of the high stress regime. On the higher end ($\tau \approx \tau_p$) Mori and Kato [130] used a third order polynomial to describe the energy of a bulging dislocation, which in connection with an Eshelby potential reduces to [115]:

$$U_b = \frac{12}{5}U_k\left(\frac{2}{3}\left(1 - \frac{\tau}{\tau_p}\right)\right)^{5/4} \tag{A6}$$

where U_k is the energy of a single kink. Continuing with the Eshelby potential, where:

$$U_k = 0.943h(E_0\Delta E)^{\frac{1}{2}} \tag{A7}$$

with the ground state energy $E_0 \approx \mu b^2/2$ and the $\Delta E - \tau_p$ relation stated above, one can differentiate the activation volume to:

$$v_{cb,\ higher\ stress}\left[b^3\right] = -\left(\frac{\partial U_b}{\partial \tau}\right)_{T=const.} = 4.63f^{\frac{3}{2}}\left(1 - \frac{\tau}{\tau_p}\right)^{1/4} \tag{A8}$$

The two solutions for the higher and lower ends of the high stress regime allow to approximate a border for the activation volume by assuming a linear inverse weighting of both solutions (see Fig. 8).

Temperature-stress relationship

To describe the temperature dependence of the activation volume, a relationship between the applied shear stress τ and the temperature T needs to be determined. Suzuki et al. [119] suggested a train of thought which leads to a scaling relationship between a function of the thermally activatable part of the resolved shear stress τ^* over τ_p and the temperature:

$$f\left(\frac{\tau^*}{\tau_p}\right) = \frac{1.11\alpha}{C\sqrt{\gamma}}\ \frac{kT}{b^3\sqrt{\tau_p K_T}} \tag{A9}$$

Here α, C and γ are material specific constants, k is Boltzmann's constant and K_T is the line tension pre-factor. Suzuki et al. calculated K_T for various bcc transition metals and found through literature study that: $\alpha = 27-30$, $\gamma = 0.7-0.9$ and C is in the order of unity. However, the exact function $f(\tau^*/\tau_p)$ is unknown, but to the fact that it is a decreasing function from $f(0) = 1$ to $f(1) = 0$. Under the assumption of a monotonic decrease one can expect a function $f(x) = (1\text{-}x)^n$, with $x = \tau^*/\tau_p$ to approximate the shape by varying the exponent n. Furthermore, it is common to normalize the temperature by a critical temperature T_C, which in this case can be calculated by:

$$T_c = \frac{b^3\sqrt{\tau_p K_T}}{\omega k}\ with\ \omega = \frac{1.11\alpha}{C\sqrt{\gamma}} \tag{A10}$$

Assuming the lower and upper bounds for all pre-factors, one arrives at $\omega_{min} = 31.6$, $\omega_{max} = 39.8$ and $\omega_{avg} = 35.7$, for the minimum, maximum and average, respectively. Thus, we get an upper (T_{CU}), lower (T_{CL}) and average (T_C) value for the critical temperature. Considering all of the above we can write:

$$\frac{\tau^*}{\tau_p} = 1 - \left(\frac{T}{T_c}\right)^{\frac{1}{n}} \tag{A11}$$

Taking into account the literature data provided by Suzuki et al. [119], as well as data by Brunner for high purity tungsten single crystals [120], a lower and upper border for this relationship can be estimated by $\tau^*/\tau_p = 1\text{-}(T/T_{CL})^{0.4}$ and $\tau^*/\tau_p = 1\text{-}(T/T_{CU})^{0.6}$, respectively.

Fig. A2 shows the literature data for Fe [121,122], Mo [120, private communication], Nb [123], Ta [124,125], reproduced from Suzuki et al. [119] and for W by Brunner [120] in connection with the lower and upper bounds suggested above. Considering that the athermal part of the Peierls stress for high purity bcc metals is only in the range of several MPa, the suggested relationships are a good approximation for the resolved shear stress over temperature behaviour thereof.

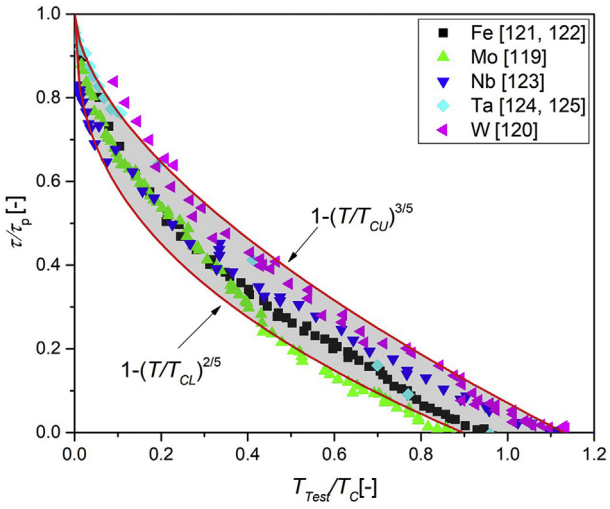

Fig. A2. Relationship of τ/τ_p versus T_{Test}/T_C with data for various bcc transition metals, reproduced from Suzuki et al. [119] and Brunner [120], with the suggested upper and lower bounds for the mathematical description.

Activation volume over temperature and high stress – low stress transition

So far, the train of thought leads to a formulation for the activation volume over temperature in the range from 0 K to the respective critical temperatures where the thermally activatable part of the Peierls stress vanishes. However, one open parameter remains, namely the kink height h. It is commonly known that screw dislocations in bcc metals can operate on three distinct glide plains ({110}, {$\bar{1}$12} and {$\bar{1}$23}) with the same <111> pencil glide direction. Thus, the kink height is dependent on the activated slip system. In the low temperature (critical bulge) regime, mainly the {011}<111> system is active, whereas closer to the critical temperature (interacting kinks) also the other systems can be activated. Table A1 summarizes the kink heights in units of the unit cell size a_0 and in units of b taken from Weinberger et al. [126], as well as the resultant pre-factor $f^{3/2}$ for all possible slip systems.

Table A1
Kink heights and pre-factors for different slip systems.

Slip system	h [a_0]	h [b]	$f^{3/2}$
{011}<111>	$\sqrt{2/3}$	$\frac{2}{3}\sqrt{2}$	0.92
{$\bar{1}$12}<111>	$\sqrt{2}$	$2\sqrt{2/3}$	2.09
{$\bar{1}$23}<111>	$\sqrt{8/3}$	$\frac{4}{3}\sqrt{2}$	2.59

The transition between high stress and low stress regime is not straightforward, as there is a regime in which neither the critical bulge nor the interacting kinks model is valid, namely:

$$\tau_{cb,min} = \frac{\Delta E}{hb} < \textit{undefined regime} < \frac{\Delta E}{2\pi hb} = \tau_{ik,max} \qquad \text{(A12)}$$

Considering again an Eshelby potential, one can calculate a maximum allowed shear stress for the interacting kinks model to be 0.052 τ_p, which translates to ~0.8 T_C. The minimum allowed shear stress for the critical bulge model is 0.325 τ_p, which relates to ~0.35 T_C.

It is acknowledged that all of the above is not a universally exact evaluation, but a mathematical consideration for the relation between activation volume and temperature in highly pure materials which are known to deform by a double kink mechanism (e.g. transition bcc metals), as studied in this work.

References

[1] M.D. Uchic, D.M. Dimiduk, J.N. Florando, W.D. Nix, Sample dimensions influence strength and crystal plasticity, Science (80-.) 305 (2004) 986–989, https://doi.org/10.1126/science.1098993.
[2] O. Kraft, P.A. Gruber, R. Mönig, D. Weygand, Plasticity in confined dimensions, Annu. Rev. Mater. Res. 40 (2010) 293–317, https://doi.org/10.1146/annurev-matsci-082908-145409.
[3] D. Kiener, C. Motz, T. Schöberl, M. Jenko, G. Dehm, Determination of mechanical properties of copper at the micron scale, Adv. Eng. Mater. 8 (2006) 1119–1125, https://doi.org/10.1002/adem.200600129.
[4] D. Kiener, C. Motz, G. Dehm, Micro-compression testing: a critical discussion of experimental constraints, Mater. Sci. Eng. A 505 (2009) 79–87, https://doi.org/10.1016/j.msea.2009.01.005.
[5] M. Legros, D.S. Gianola, C. Motz, Quantitative in situ mechanical testing in electron microscopes, MRS Bull. 35 (2010) 354–360, https://doi.org/10.1557/mrs2010.567.
[6] D.S. Gianola, C. Eberl, Micro- and nanoscale tensile testing of materials, J. Mater. 61 (2009) 24–35, https://doi.org/10.1007/s11837-009-0037-3.
[7] J.R. Greer, J.T.H. De Hosson, J.T.M. De Hosson, Plasticity in small-sized metallic systems: intrinsic versus extrinsic effect, Prog. Mater. Sci. 56 (2011) 654–724, https://doi.org/10.1016/j.pmatsci.2011.01.005.
[8] S.W. Lee, W.D. Nix, Size dependence of the yield strength of fcc and bcc metallic micropillars with diameters of a few micrometers, Philos. Mag. 92 (2012) 1238–1260, https://doi.org/10.1080/14786435.2011.643250.
[9] Z.-W. Shan, R.K. Mishra, S.A. Syed Asif, O.L. Warren, A.M. Minor, Mechanical annealing and source-limited deformation in submicrometre-diameter Ni crystals, Nat. Mater. 7 (2007) 115–119, https://doi.org/10.1038/nmat2085.
[10] C. Zhou, I.J. Beyerlein, R. LeSar, Plastic deformation mechanisms of fcc single crystals at small scales, Acta Mater. 59 (2011) 7673–7682, https://doi.org/10.1016/j.actamat.2011.08.032.
[11] J.M. Wheeler, C. Kirchlechner, J.S. Micha, J. Michler, D. Kiener, The effect of size on the strength of FCC metals at elevated temperatures: annealed copper, Philos. Mag. (2016) 1–17, https://doi.org/10.1080/14786435.2016.1224945.
[12] J.-Y. Kim, D. Jang, J.R. Greer, Tensile and compressive behavior of tungsten, molybdenum, tantalum and niobium at the nanoscale, Acta Mater. 58 (2010) 2355–2363, https://doi.org/10.1016/j.actamat.2009.12.022.
[13] D. Kaufmann, R. Mönig, C.A. Volkert, O. Kraft, Size dependent mechanical behaviour of tantalum, Int. J. Plast. 27 (2011) 470–478, https://doi.org/10.1016/j.ijplas.2010.08.008.
[14] A.S. Schneider, C.P. Frick, E. Arzt, W.J. Clegg, S. Korte, Influence of test temperature on the size effect in molybdenum small-scale compression pillars, Phil. Mag. Lett. 93 (2013) 331–338, https://doi.org/10.1080/09500839.2013.777815.
[15] S.-W. Lee, Y. Cheng, I. Ryu, J.R. Greer, Cold-temperature deformation of nanosized tungsten and niobium as revealed by in-situ nano-mechanical experiments, Sci. China Technol. Sci. 57 (2014) 652–662, https://doi.org/10.1007/s11431-014-5502-8.
[16] A.B. Hagen, C. Thaulow, Low temperature in-situ micro-compression testing of iron pillars, Mater. Sci. Eng. A 678 (2016) 355–364, https://doi.org/10.1016/j.msea.2016.09.110.
[17] B.R.S. Rogne, C. Thaulow, Strengthening mechanisms of iron micropillars, Philos. Mag. (2014) 1–15, https://doi.org/10.1080/14786435.2014.984004.
[18] S.M. Han, T. Bozorg-Grayeli, J.R. Groves, W.D. Nix, Size effects on strength and plasticity of vanadium nanopillars, Scripta Mater. 63 (2010) 1153–1156, https://doi.org/10.1016/j.scriptamat.2010.08.011.
[19] O. Torrents Abad, J.M. Wheeler, J. Michler, A.S. Schneider, E. Arzt, Temperature-dependent size effects on the strength of Ta and W micropillars, Acta Mater. 103 (2016) 483–494, https://doi.org/10.1016/j.actamat.2015.10.016.
[20] T.A. Parthasarathy, S.I. Rao, D.M. Dimiduk, M.D. Uchic, D.R. Trinkle, Contribution to size effect of yield strength from the stochastics of dislocation source lengths in finite samples, Scripta Mater. 56 (2007) 313–316, https://doi.org/10.1016/j.scriptamat.2006.09.016.
[21] J.A. El-Awady, Unravelling the physics of size-dependent dislocation-mediated plasticity, Nat. Commun. 6 (2015) 5926, https://doi.org/10.1038/ncomms6926.
[22] A.S. Schneider, B.G. Clark, C.P. Frick, P.A. Gruber, E. Arzt, Effect of orientation and loading rate on compression behavior of small-scale molybdenum pillars, Mater. Sci. Eng A. 508 (2009) 241–246.
[23] A.S. Schneider, C.P. Frick, B.G. Clark, P.A. Gruber, E. Arzt, Influence of orientation on the size effect in bcc pillars with different critical temperatures, Mater. Sci. Eng. A 528 (2011) 1540–1547, https://doi.org/10.1016/j.msea.2010.10.073.
[24] B.R.S. Rogne, C. Thaulow, Effect of crystal orientation on the strengthening of iron micro pillars, Mater. Sci. Eng. A 621 (2015) 133–142, https://doi.org/10.1016/j.msea.2014.10.067.
[25] H. Bei, S. Shim, G.M. Pharr, E.P. George, Effects of pre-strain on the

compressive stress-strain response of Mo-alloy single-crystal micropillars, Acta Mater. 56 (2008) 4762–4770, https://doi.org/10.1016/j.actamat.2008.05.030.
[26] A.S. Schneider, D. Kiener, C.M. Yakacki, H.J. Maier, P.A. Gruber, N. Tamura, M. Kunz, A.M. Minor, C.P. Frick, Influence of bulk pre-straining on the size effect in nickel compression pillars, Mater. Sci. Eng. A 559 (2013) 147–158, https://doi.org/10.1016/j.msea.2012.08.055.
[27] J.A. El-Awady, M.D. Uchic, P.A. Shade, S.-L. Kim, S.I. Rao, D.M. Dimiduk, C. Woodward, Pre-straining effects on the power-law scaling of size-dependent strengthening in Ni single crystals, Scripta Mater. 68 (2013) 207–210, https://doi.org/10.1016/j.scriptamat.2012.10.035.
[28] H. Conrad, Thermally activated deformation of metals, JMET (J. Med. Eng. Technol.) (1964) 582–588, https://doi.org/10.1007/BF03378292.
[29] B. Sestak, A. Seeger, Gleitung und Verfestigung in kubisch-raumzentrierten Metallen und Legierungen, Zeitschrift Für Met. 69 (1978) 195–202.
[30] A.S. Schneider, D. Kaufmann, B.G. Clark, C.P. Frick, P.A. Gruber, R. Mönig, O. Kraft, E. Arzt, Correlation between critical temperature and strength of small-scale bcc pillars, Phys. Rev. Lett. 103 (2009) 105501, https://doi.org/10.1103/PhysRevLett.103.105501.
[31] J.Y. Zhang, X. Liang, P. Zhang, K. Wu, G. Liu, J. Sun, Emergence of external size effects in the bulk-scale polycrystal to small-scale single-crystal transition: a maximum in the strength and strain-rate sensitivity of multicrystalline Cu micropillars, Acta Mater. 66 (2014) 302–316, https://doi.org/10.1016/j.actamat.2013.11.018.
[32] Y. Xiao, J. Wehrs, H. Ma, T. Al-Samman, S. Korte-Kerzel, M. Göken, J. Michler, R. Spolenak, J.M. Wheeler, Investigation of the deformation behavior of aluminum micropillars produced by focused ion beam machining using Ga and Xe ions, Scripta Mater. 127 (2017), https://doi.org/10.1016/j.scriptamat.2016.08.028.
[33] A.T. Jennings, M.J. Burek, J.R. Greer, Microstructure versus size and mechanical properties of electroplated and single crystalline Cu nanopillars, PRL 104 (2010) 135503, https://doi.org/10.1103/PhysRevLett.104.135503.
[34] D. Kiener, C. Motz, M. Rester, M. Jenko, G. Dehm, FIB damage of Cu and possible consequences for miniaturized mechanical tests, Mater. Sci. Eng. A 459 (2007) 262–272, https://doi.org/10.1016/j.msea.2007.01.046.
[35] P.J.M. Janssen, J.P.M. Hoefnagels, T.H. de Keijser, M.G.D. Geers, Processing induced size effects in plastic yielding upon miniaturisation, J. Mech. Phys. Solid. 56 (2008) 2687–2706, https://doi.org/10.1016/j.jmps.2008.03.008.
[36] A.S. Argon, S.R. Maloof, Plastic deformation of tungsten single crystals at low temperatures, Acta Metall. 14 (1966) 1449–1462, https://doi.org/10.1016/0001-6160(66)90165-9.
[37] D. Brunner, V. Glebovsky, Plastic properties of high-purity W single crystals, Mater. Lett. 42 (2000) 290–296, https://doi.org/10.1016/S0167-577X(99)00200-1.
[38] D. Brunner, Comparison of Flow Stress Measurements on high purity tungsten single crystals with the kink pair theory, JIM, Mater. Trans. 41 (2000) 152–160.
[39] D. Brunner, V. Glebovsky, Analysis of flow-stress measurements of high purity tungsten single crystals, Mater. Lett. 44 (2000) 144–152, https://doi.org/10.1016/S0167-577X(00)00017-3.
[40] D. Brunner, Temperature dependence of the plastic flow of high-purity tungsten single crystals, Int. J. Mater. Res. 101 (2010) 1003–1013, https://doi.org/10.3139/146.110362.
[41] D. Cereceda, M. Diehl, F. Roters, D. Raabe, J.M. Perlado, J. Marian, Unraveling the temperature dependence of the yield strength in single-crystal tungsten using atomistically-informed crystal plasticity calculations, Int. J. Plast. 78 (2016) 242–265, https://doi.org/10.1016/j.ijplas.2015.09.002.
[42] Q. Wei, T. Jiao, K.T. Ramesh, E. Ma, L.J. Kecskes, L. Magness, R. Dowding, V.U. Kazykhanov, R.Z. Valiev, Mechanical behavior and dynamic failure of high-strength ultrafine grained tungsten under uniaxial compression, Acta Mater. 54 (2006) 77–87.
[43] Z. Li, C. Hou, M. Huang, C. Ouyang, Strengthening mechanism in micro-polycrystals with penetrable grain boundaries by discrete dislocation dynamics simulation and Hall-Petch effect, Comput. Mater. Sci. 46 (2009) 1124–1134, https://doi.org/10.1016/j.commatsci.2009.05.021.
[44] S. Saha, M.A. Motalab, M. Mahboob, Investigation on mechanical properties of polycrystalline W nanowire, Comput. Mater. Sci. 136 (2017) 52–59, https://doi.org/10.1016/j.commatsci.2017.04.025.
[45] R. Fritz, V. Maier-Kiener, D. Lutz, D. Kiener, Interplay between sample size and grain size: single crystalline vs. ultrafine-grained chromium micropillars, Mater. Sci. Eng. A 674 (2016) 626–633, https://doi.org/10.1016/j.msea.2016.08.015.
[46] S. Schreijäg, D. Kaufmann, M. Wenk, O. Kraft, R. Mönig, Size and microstructural effects in the mechanical response of alpha-Fe and low alloyed steel, Acta Mater. 97 (2015) 94–104, https://doi.org/10.1016/j.actamat.2015.06.038.
[47] P.J. Imrich, C. Kirchlechner, D. Kiener, G. Dehm, In situ TEM micro-compression of single and bicrystalline samples: insights and limitations, JOM (J. Occup. Med.) 67 (2015) 1704–1712, https://doi.org/10.1007/s11837-015-1440-6.
[48] N. Kheradmand, H. Vehoff, A. Barnoush, An insight into the role of the grain boundary in plastic deformation by means of a bicrystalline pillar compression test and atomistic simulation, Acta Mater. 61 (2013) 7454–7465, https://doi.org/10.1016/j.actamat.2013.08.056.
[49] N.V. Malyar, G. Dehm, C. Kirchlechner, Strain rate dependence of the slip transfer through a penetrable high angle grain boundary in copper, Scripta Mater. 138 (2017) 88–91, https://doi.org/10.1016/j.scriptamat.2017.05.042.
[50] N.V. Malyar, J.S. Micha, G. Dehm, C. Kirchlechner, Size effect in bi-crystalline micropillars with a penetrable high angle grain boundary, Acta Mater. 129 (2017) 312–320, https://doi.org/10.1016/j.actamat.2017.03.003.
[51] J.A. El-Awady, S.I.S.I. Rao, C. Woodward, D.M.M. Dimiduk, M.D.D. Uchic, Trapping and escape of dislocations in micro-crystals with external and internal barriers, Int. J. Plast. 27 (2011) 372–387, https://doi.org/10.1016/j.ijplas.2010.06.006.
[52] K.S. Ng, A.H.W. Ngan, Effects of trapping dislocations within small crystals on their deformation behavior, Acta Mater. 57 (2009) 4902–4910, https://doi.org/10.1016/j.actamat.2009.06.053.
[53] D. Caillard, Kinetics of dislocations in pure Fe. Part II. In situ straining experiments at low temperature, Acta Mater. 58 (2010) 3504–3515, https://doi.org/10.1016/j.actamat.2010.02.024.
[54] V. Maier, A. Hohenwarter, R. Pippan, D. Kiener, Thermally activated deformation processes in body-centered cubic Cr – how microstructure influences strain-rate sensitivity, Scripta Mater. 106 (2015) 42–45, https://doi.org/10.1016/j.scriptamat.2015.05.001.
[55] R. Fritz, D. Wimler, A. Leitner, V. Maier-Kiener, D. Kiener, Dominating deformation mechanisms in ultrafine-grained chromium across length scales and temperatures, Acta Mater. 140 (2017) 176–187, https://doi.org/10.1016/j.actamat.2017.08.043.
[56] V.G. Glebovsky, V.N. Semenov, V. V Lomeyko, Influence of the crystallization conditions on the structural perfection of Mo and W single crystals, J. Cryst. Growth 87 (1988) 142–150, https://doi.org/10.1016/0022-0248(88)90353-3.
[57] S. Wurster, C. Motz, R. Pippan, Characterization of the fracture toughness of micro-sized tungsten single crystal notched specimens, Philos. Mag. 92 (2012) 1803–1825, https://doi.org/10.1080/14786435.2012.658449.
[58] R. Pippan, S. Scheriau, A. Taylor, M. Hafok, A. Hohenwarter, A. Bachmaier, Saturation of fragmentation during severe plastic deformation, Annu. Rev. Mater. Res. 40 (2010) 319–343, https://doi.org/10.1146/annurev-matsci-070909-104445.
[59] R.Z. Valiev, R.K. Islamgaliev, I.V. Alexandrov, Bulk nanostructured materials from severe plastic deformation, Prog. Mater. Sci. 45 (45) (2000) 103–189.
[60] A.V. Ganeev, R.K. Islamgaliev, R.Z. Valiev, Refinement of tungsten microstructure upon severe plastic deformation, Phys. Met. Metallogr. 115 (2014) 139–145, https://doi.org/10.1134/S0031918X14020070.
[61] L.J. Kecskes, K.C. Cho, R.J. Dowding, B.E. Schuster, R.Z. Valiev, Q. Wei, Grain size engineering of bcc refractory metals: top-down and bottom-up-Application to tungsten, Mater. Sci. Eng. A 467 (2007) 33–43, https://doi.org/10.1016/j.msea.2007.02.099.
[62] Q. Wei, H.T. Zhang, B.E. Schuster, K.T. Ramesh, R.Z. Valiev, L.J. Kecskes, R.J. Dowding, L. Magness, K. Cho, Microstructure and mechanical properties of super-strong nanocrystalline tungsten processed by high-pressure torsion, Acta Mater. 54 (2006) 4079–4089, https://doi.org/10.1016/j.actamat.2006.05.005.
[63] S. Wurster, R. Treml, R. Fritz, M.W. Kapp, E.-M. Langs, M. Alfreider, C. Ruhs, P.J. Imrich, G. Felber, D. Kiener, Novel methods for the site specific preparation of micromechanical structures, Prakt. Met. Sonderband. 46 (2014) 27–36, https://doi.org/10.3139/147.110331.
[64] D. Kiener, C. Motz, G. Dehm, R. Pippan, Overview on established and novel FIB based miniaturized mechanical testing using in-situ SEM, Int. J. Mat. Res. 100 (2009) 1074–1087, https://doi.org/10.3139/146.110149.
[65] R. Fritz, D. Kiener, Development and application of a heated in-situ SEM micro-testing device, Measurement 110 (2017) 356–366, https://doi.org/10.1016/j.measurement.2017.07.012.
[66] I.N. Sneddon, The relation between load and penetration in the axisymmetric boussinesq problem for a punch of arbitrary profile, Int. J. Eng. Sci. 3 (1965) 47–57, https://doi.org/10.1016/0020-7225(65)90019-4.
[67] D. Kiener, W. Grosinger, G. Dehm, On the importance of sample compliance in uniaxial microtesting, Scripta Mater. 60 (2009) 148–151, https://doi.org/10.1016/j.scriptamat.2008.09.024.
[68] D. Tabor, The Hardness of Metals, OUP, Oxford, 1951.
[69] A. Leitner, V. Maier-Kiener, D. Kiener, Extraction of flow behavior and Hall-Petch parameters using a nanoindentation multiple sharp tip Approach, Adv. Eng. Mater. (2016) 1–9, https://doi.org/10.1002/adem.201600669.
[70] V. Maier, K. Durst, J. Mueller, B. Backes, H.W. Höppel, M. Göken, Nanoindentation strain-rate jump tests for determining the local strain-rate sensitivity in nanocrystalline Ni and ultrafine-grained Al, J. Mater. Res. 26 (2011) 1421–1430, https://doi.org/10.1557/jmr.2011.156.
[71] W.C. Oliver, G.M. Pharr, An improved technique for determining hardness and elastic modulus using load and displacement sensing indentation experiments, J. Mater. Res. 7 (1992) 1564–1583. https://doi.org/10.1557/JMR.1992.1564.
[72] V. Maier, A. Leitner, R. Pippan, D. Kiener, Thermally activated deformation behavior of ufg-Au: environmental issues during long-term and high-temperature nanoindentation testing, JOM (J. Occup. Med.) 67 (2015) 2934–2944, https://doi.org/10.1007/s11837-015-1638-7.
[73] A.G. Atkins, D. Tabor, Plastic indentation in metals with cones, J. Mech. Phys. Solid. 13 (1965) 149–164, https://doi.org/10.1016/0022-5096(65)90018-9.
[74] W.D. Nix, H. Gao, Indentation size effects in crystalline materials: a law for strain gradient plasticity, J. Mech. Phys. Solid. 46 (1998) 411–425, https://doi.org/10.1016/S0022-5096(97)00086-0.
[75] E. Grünwald, R. Nuster, R. Treml, D. Kiener, G. Paltauf, R. Brunner, Young's

modulus and Poisson's ratio characterization of tungsten thin films via laser ultrasound, Mater. Today Proc. 2 (2015) 4289–4294, https://doi.org/10.1016/j.matpr.2015.09.015.
[76] P. Gumbsch, J. Riedle, A. Hartmaier, H.F. Fischmeister, Controlling factors for the brittle-to-ductile transition temperature in tungsten single crystals, Science (80-.) 282 (1998) 1293–1295, https://doi.org/10.1126/science.282.5392.1293.
[77] P. Gumbsch, Brittle fracture and the brittle-to-ductile transition of tungsten, J. Nucl. Mater. 323 (2003) 304–312, https://doi.org/10.1016/j.jnucmat.2003.08.009.
[78] M. Faleschini, H. Kreuzer, D. Kiener, R. Pippan, Fracture toughness investigations of tungsten alloys and SPD tungsten alloys, J. Nucl. Mater. 367–370 (2007) 800–805, https://doi.org/10.1016/j.jnucmat.2007.03.079.
[79] J. Reiser, J. Hoffmann, U. Jäntsch, M. Klimenkov, S. Bonk, C. Bonnekoh, M. Rieth, A. Hoffmann, T. Mrotzek, Ductilisation of tungsten (W): on the shift of the brittle-to-ductile transition (BDT) to lower temperatures through cold rolling, Int. J. Refract. Metals Hard Mater. 54 (2016) 351–369, https://doi.org/10.1016/j.ijrmhm.2015.09.001.
[80] Q. Wei, Strain rate effects in the ultrafine grain and nanocrystalline regimes-influence on some constitutive responses, J. Mater. Sci. 42 (2007) 1709–1727, https://doi.org/10.1007/s10853-006-0700-9.
[81] M.J. Marcinkowski, H.A. Lipsitt, The plastic deformation of Chromium at low temperatures, Acta Metall. 10 (1962) 95–111, https://doi.org/10.1016/0001-6160(62)90055-X.
[82] K. Leitner (née Babinsky), P.J. Felfer, D. Holec, J. Cairney, W. Knabl, A. Lorich, H. Clemens, S. Primig, On grain boundary segregation f molybdenum materials, Mater. Des. 135 (2017) 204–212, https://doi.org/10.1016/j.matdes.2017.09.019.
[83] B. Merle, V. Maier-Kiener, G.M. Pharr, Influence of modulus-to-hardness ratio and harmonic parameters on continuous stiffness measurement during nanoindentation, Acta Mater. 134 (2017) 167–176, https://doi.org/10.1016/j.actamat.2017.05.036.
[84] A. Leitner, V. Maier-Kiener, D. Kiener, Dynamic nanoindentation testing: is there an influence on a material's hardness? Mater. Res. Lett. 5 (2017) 485–493, https://doi.org/10.1080/21663831.2017.1331384, submitted.
[85] K.L. Johnson, The correlation of indentation experiments, J. Mech. Phys. Solid. 18 (1970) 115–126. https://doi.org/10.1016/0022-5096(70)90029-3.
[86] M. Mata, O. Casals, J. Alcalá, The plastic zone size in indentation experiments: the analogy with the expansion of a spherical cavity, Int. J. Solid Struct. 43 (2006) 5994–6013, https://doi.org/10.1016/j.ijsolstr.2005.07.002.
[87] K. Zhang, J.R. Weertman, J.A. Eastman, Rapid stress-driven grain coarsening in nanocrystalline Cu at ambient and cryogenic temperatures, Appl. Phys. Lett. 87 (2005), https://doi.org/10.1063/1.2008377.
[88] E.O. Hall, The deformation and ageing of mild steel: III discussion of results, Proc. Phys. Soc. B 64 (1951) 747–753.
[89] N.J. Petch, The cleavage strength of polycrystals, J. Iron Steel Instruments. 174 (1953) 25–28.
[90] G.M. Le, A. Godfrey, N. Hansen, W. Liu, G. Winther, X. Huang, Influence of grain size in the near-micrometre regime on the deformation microstructure in aluminium, Acta Mater. 61 (2013) 7072–7086, https://doi.org/10.1016/j.actamat.2013.07.046.
[91] Y.Z. Tian, S. Gao, L.J. Zhao, S. Lu, R. Pippan, Z.F. Zhang, N. Tsuji, Remarkable transitions of yield behavior and Lüders deformation in pure Cu by changing grain sizes, Scripta Mater. 142 (2018) 88–91, https://doi.org/10.1016/j.scriptamat.2017.08.034.
[92] F. Mompiou, M. Legros, a. Boé, M. Coulombier, J.P. Raskin, T. Pardoen, Inter- and intragranular plasticity mechanisms in ultrafine-grained Al thin films: an in situ TEM study, Acta Mater. 61 (2013) 205–216, https://doi.org/10.1016/j.actamat.2012.09.051.
[93] G.M. Cheng, W.W. Jian, W.Z. Xu, H. Yuan, P.C. Millett, Y.T. Zhu, Grain size effect on deformation mechanisms of nanocrystalline bcc metals, Mater. Res. Lett. 1 (2013) 26–31, https://doi.org/10.1080/21663831.2012.739580.
[94] X. Huang, N. Hansen, N. Tsuji, Hardening by annealing and softening by deformation in nanostructured metals, Science (80-.) 312 (2006) 249–251, https://doi.org/10.1126/science.1124268.
[95] V. Samaee, R. Gatti, B. Devincre, T. Pardoen, D. Schryvers, H. Idrissi, Dislocation driven nanosample plasticity: new insights from quantitative in-situ TEM tensile testing, Sci. Rep. 8 (2018) 12012, https://doi.org/10.1038/s41598-018-30639-8.
[96] S.H. Oh, M. Legros, D. Kiener, G. Dehm, In situ observation of dislocation nucleation and escape in a submicrometre aluminium single crystal, Nat. Mater. 8 (2009) 95–100, https://doi.org/10.1038/nmat2370.
[97] P.J. Imrich, C. Kirchlechner, D. Kiener, G. Dehm, Internal and external stresses: in situ TEM compression of Cu bicrystals containing a twin boundary, Scripta Mater. 100 (2015) 94–97, https://doi.org/10.1016/j.scriptamat.2014.12.023.
[98] A.A.N. Nemeth, J. Reiser, D.E.J. Armstrong, M. Rieth, The nature of the brittle-to-ductile transition of ultra fine grained tungsten (W) foil, Int. J. Refract. Metals Hard Mater. 50 (2015) 9–15, https://doi.org/10.1016/j.ijrmhm.2014.11.005.
[99] B. Yang, C. Motz, W. Grosinger, G. Dehm, Cyclic loading behavior of micro-sized polycrystalline copper wires, Procedia Eng 2 (2010) 925–930, https://doi.org/10.1016/j.proeng.2010.03.100.
[100] B. Yang, C. Motz, M. Rester, G. Dehm, Yield stress influenced by the ratio of wire diameter to grain size - a competition between the effects of specimen microstructure and dimension in micro-sized polycrystalline copper wires, Philos. Mag. 92 (2012) 3243–3256, https://doi.org/10.1080/14786435.2012.693215.
[101] D. Wu, X.L. Wang, T.G. Nieh, Variation of strain rate sensitivity with grain size in Cr and other body-centred cubic metals, J. Phys. D Appl. Phys. 47 (2014) 175303, https://doi.org/10.1088/0022-3727/47/17/175303.
[102] M.W. Kapp, C. Kirchlechner, R. Pippan, G. Dehm, Importance of dislocation pile-ups on the mechanical properties and the Bauschinger effect in micro-cantilevers, J. Mater. Res. 30 (2015) 791–797, https://doi.org/10.1557/jmr.2015.49.
[103] N.Q. Chinh, T. Csanadi, J. Gubicza, R.Z. Valiev, B.B. Straumal, T.G. Langdon, The effect of grain boundary sliding and strain rate sensitivity on the ductility of ultrafine-grained materials, MSF 667–669 (2010) 677–682, https://doi.org/10.4028/www.scientific.net/msf.667-669.677.
[104] T.G. Langdon, Grain boundary sliding revisited: developments in sliding over four decades, J. Mater. Sci. 41 (2006) 597–609, https://doi.org/10.1007/s10853-006-6476-0.
[105] A. Seeger, The temperature and strain rate dependence of the flow stress of BCC metals: a theory based on the kink-kink interactions, Z. Met. 72 (1981) 369–380. http://www.scopus.com/inward/record.url?eid=2-s2.0-0019573211&partnerID=40&md5=501f3beb194c5d6595ab99560067629c.
[106] J. Wehrs, G. Mohanty, G. Guillonneau, A.A. Taylor, X. Maeder, D. Frey, L. Philippe, S. Mischler, J.M. Wheeler, J. Michler, Comparison of in situ micromechanical strain-rate sensitivity measurement techniques, JOM (J. Occup. Med.) 67 (2015) 1684–1693, https://doi.org/10.1007/s11837-015-1447-z.
[107] J. May, H.W. Höppel, M. Göken, Strain rate sensitivity of ultrafine-grained aluminium processed by severe plastic deformation, Scripta Mater. 53 (2005) 189–194, https://doi.org/10.1016/j.scriptamat.2005.03.043.
[108] J.Y. Zhang, G. Liu, J. Sun, Strain rate effects on the mechanical response in multi- and single-crystalline Cu micropillars: grain boundary effects, Int. J. Plast. 50 (2013) 1–17, https://doi.org/10.1016/j.ijplas.2013.03.009.
[109] O. Renk, V. Maier-Kiener, I. Issa, J.H. Li, D. Kiener, R. Pippan, Anneal hardening and elevated temperature strain rate sensitivity of nanostructured metals: their relation to intergranular dislocation accommodation, Acta Mater. 165 (2018) 409–419, https://doi.org/10.1016/J.ACTAMAT.2018.12.002.
[110] Q. Wei, S. Cheng, K.T. Ramesh, E. Ma, Effect of nanocrystalline and ultrafine grain sizes on the strain rate sensitivity and activation volume-FCC vs BCC metals.pdf, Mater. Sci. Eng. A 381 (2004) 71–79.
[111] Q. Zhou, J. Zhao, J.Y. Xie, F. Wang, P. Huang, T.J. Lu, K.W. Xu, Grain size dependent strain rate sensitivity in nanocrystalline body-centered cubic metal thin films, Mater. Sci. Eng. A 608 (2014) 184–189, https://doi.org/10.1016/j.msea.2014.04.080.
[112] V. Maier, C. Schunk, M. Göken, K. Durst, Microstructure-dependent deformation behaviour of bcc-metals – indentation size effect and strain rate sensitivity, Philos. Mag. 95 (2014) 1766–1779, https://doi.org/10.1080/14786435.2014.982741.
[113] I.-C. Choi, C. Brandl, R. Schwaiger, Thermally activated dislocation plasticity in body-centered cubic chromium studied by high-temperature nano-indentation, Acta Mater. 140 (2017) 107–115, https://doi.org/10.1016/j.actamat.2017.08.026.
[114] J.W. Christian, B.C. Masters, Low-temperature deformation of body-centred cubic metals. I. yield and flow stress measurements, Proc. R. Soc. London. Ser. A 281 (1964) 223–239, https://doi.org/10.1098/rspa.1964.0179.
[115] D. Caillard, J.L. Martin, Thermally Activated Mechanisms in Crystal Plasticity, EPFL, Elsevier, Lausanne, Switzerland, 2003, https://doi.org/10.1016/S1470-1804(03)X8028-1.
[116] J.P. Hirth, J. Lothe, T. Mura, Theory of Dislocations, second ed., Wiley & Sons, 1983 https://doi.org/10.1115/1.3167075.
[117] A. Seeger, Dislocations 1984, in: P. Veyssiere, L. Kubin, J. Castaing (Eds.), C.N.R.S. Paris, 1984, pp. 141–178.
[118] J.D. Eshelby, The interaction of kinks and elastic waves, Proc. R. Soc. A Math. Phys. Eng. Sci. 266 (1962) 222–246, https://doi.org/10.1098/rspa.1962.0058.
[119] T. Suzuki, Y. Kamimura, H.O.K. Kirchner, Plastic homology of bcc metals, Philos. Mag. A 79 (1999) 1629–1642, https://doi.org/10.1080/01418619908210383.
[120] D. Brunner, Comparison of flow-stress measurements on high-purity tungsten single crystals with the kink-pair theory, Mater. Trans. 41 (2000) 152–160, https://doi.org/10.2320/matertrans1989.41.152.
[121] E. Kuramoto, Y. Aono, K. Kitajima, Thermally activated slip deformation of high purity iron single crystals between 4.2 K and 300 K, Scripta Metall. 13 (1979) 1039–1042, https://doi.org/10.1016/0036-9748(79)90199-6.
[122] Y. Aono, E. Kuramoto, K. Kitajima, Plastic deformation of high-purity iron, in: R.C. Gifkins (Ed.), Proceeding Sixth Int. Conf. Strength Met. Alloy, 1982, p. 9.
[123] S. Takeuchi, T. Hashimoto, K. Maeda, Plastic deformation of bcc metal single crystals at very low temperatures, Trans. Japan Inst. Met. 23 (1982) 60–69, https://doi.org/10.2320/matertrans1960.23.60.
[124] R. Lachenmann, H. Schultz, Experimentelle Untersuchungen zur Plastizität von Tantaleinkristallen, Z. Met. 66 (1975) 443–452.
[125] S. Takeuchi, K. Maeda, Slip in high purity tantalum between 0.7 and 40 K, Acta Metall. 25 (1977) 1485–1490, https://doi.org/10.1016/0001-6160(77)90078-5.
[126] C.R. Weinberger, B.L. Boyce, C.C. Battaile, Slip planes in bcc transition metals, Int. Mater. Rev. 58 (2013) 296–314, https://doi.org/10.1179/

1743280412y.0000000015.
[127] V. Celli, M. Kabler, T. Ninomiya, R. Thomson, Theory of dislocation mobility in semiconductors, Phys. Rev. 131 (1963) 58–72, https://doi.org/10.1103/physrev.131.58.
[128] Y. Kamimura, K. Edagawa, S. Takeuchi, Experimental evaluation of the Peierls stresses in a variety of crystals and their relation to the crystal structure, Acta Mater. 61 (2013) 294–309, https://doi.org/10.1016/j.actamat.2012.09.059.
[129] J.E. Dorn, S. Rajnak, Nucleation of kink pairs and the Peierls' mechanism of plastic deformation, Trans. Metall. Soc. AIME 230 (1964) 1052–1064.
[130] T. Mori, M. Kato, Asymptotic form of activation energy for double-kink formation in a dislocation in a one-dimensional periodic field, Philos. Mag. A 43 (1981) 1315–1320, https://doi.org/10.1080/01418618108239512.